

Article

Impact of Variable Parameters of Expansion Joints and Bearing Supports on the Vehicle-Induced Vibration of Curved Girder Bridges

Yu Zheng ^{1,2}, Chunfang Lu ^{1,2}, Xiaomin Huang ^{3,*}, Weibing Xu ⁴ , Daxing Zhou ⁵, Jin Li ⁵, Jianxiang Li ⁴, Liqun Hou ⁵, Kuan Wang ⁵ and Yulong Sun ⁵

¹ School of Mechanical, Electronic and Control Engineering, Beijing Jiaotong University, Beijing 100044, China; 19116054@bjtu.edu.cn (Y.Z.); chrmcx@sina.com (C.L.)

² China Railway Beijing Group Co., Ltd., Beijing 100038, China

³ School of Architectural Engineering, Kunming University of Science and Technology, Kunming 650032, China

⁴ Faculty of Architecture, Civil and Transportation Engineering, Beijing University of Technology, Beijing 100124, China; weibingx@bjut.edu.cn (W.X.); lijianxiang922@mails.bjut.edu.cn (J.L.)

⁵ China Railway Construction Group Co. Ltd., Beijing 100040, China; zhoudaxing@ztsj.cn (D.Z.); lijin@ztsj.cn (J.L.); houliqun@ztsj.cn (L.H.); wangkuan@ztsj.cn (K.W.); sunyulong.ztsj@crcc.cn (Y.S.)

* Correspondence: huangxm.yn@kust.edu.cn

Abstract: To study how varying the parameters of expansion joints and bearing supports (E-B parameters) affects the dynamic response of a coupled vehicle–bridge system for curved girder bridges, a dynamic response analysis method for the coupled vehicle–joint (bearing)–bridge system, which takes into account centrifugal forces, was proposed and verified. Subsequently, taking a continuous curved box girder bridge as the prototype, the influence of the E-B parameters on the vehicle-induced dynamic response of the curved girder bridge was explored. The results showed that the dynamic amplification factor (DAF) of the middle beam of the expansion joint (DAF-EJ) and the main girder of the curved bridge (DAF-MG) were both significantly influenced by the E-B parameters. When there were height differences between the middle beam and side beam in the EJ, the DAF-EJ obviously varied, and the DAF-MG increased. When the EJ was damaged, the impact effect of the vehicle on the bearing support increased. The DAF-EJ and DAF-MG both increased with the decrease of the vertical support stiffness of the bearing support. The DAF-EJ was greatly affected by the single-support void at the near-slit end of the lane. The DAF-MGs at the beam end, the 1/4 point and 1/2 point of the first span, and the 1/2 point of the second span, were significantly affected by the single-support void near the measuring point. Compared with the single-support void, the DAF-EJ and DAF-MG more significantly increased under the double-support void. Variation in the height difference of the EJ had a more significant effect on the DAF-EJ and DAF-MG at the beam end, while a vertical stiffness reduction in the bearing support had a more significant effect on the DAF-MG.

Keywords: coupled vehicle–bridge system; dynamic response; curved girder bridge; expansion joint; support; numerical simulation



Citation: Zheng, Y.; Lu, C.; Huang, X.; Xu, W.; Zhou, D.; Li, J.; Li, J.; Hou, L.; Wang, K.; Sun, Y. Impact of Variable Parameters of Expansion Joints and Bearing Supports on the Vehicle-Induced Vibration of Curved Girder Bridges. *Buildings* **2024**, *14*, 293. <https://doi.org/10.3390/buildings14010293>

Academic Editors: Binsheng (Ben) Zhang and Ehsan Noroozinejad Farsangi

Received: 7 December 2023

Revised: 16 January 2024

Accepted: 18 January 2024

Published: 22 January 2024



Copyright: © 2024 by the authors. Licensee MDPI, Basel, Switzerland. This article is an open access article distributed under the terms and conditions of the Creative Commons Attribution (CC BY) license (<https://creativecommons.org/licenses/by/4.0/>).

1. Introduction

Curved girder bridges are important components of three-dimensional urban transport systems and highway transport hubs [1,2]. Unlike normal girder bridges, the curved girder bridge is a type of irregular bridge which is usually located on a curved trajectory of a road. In this case, centrifugal forces result from the outward centrifugal acceleration of vehicles, which have potential effects on the stability and structure of the bridge. Therefore, the centrifugal forces of vehicles become critical factors in bridge design, including the design of static and dynamic bearing capacities [3,4]. Conceivably, the introduction of the centrifugal force makes the problem of the vehicle-induced dynamic response of curved

girder bridges more complicated. The expansion joint (EJ) and bearing support (BS) are important components that affect the vehicle-induced dynamic responses of curved girder bridges, and how their variable parameters influence the vehicle-induced dynamic response of curved girder bridges cannot be ignored [5–7].

In recent years, vibration analysis of coupled vehicle–bridge systems that takes into account the variable parameters of expansion joints and bearings (E-B parameters) has gradually become a research hot spot. Many researchers have carried out a series of studies to clarify the influence of E-B parameters on the response of coupled vehicle–bridge vibration. For EJ, Artmont et al. [8] improved the simulation method of the vehicle–EJ coupling contact and proposed a trapezoidal impulsive load that can consider the process of wheels passing through an EJ. Further, a three-dimensional numerical analysis model of an EJ was established, and the force and deformation characteristics of the EJ were analyzed under impulsive loads. Deng et al. [9,10] investigated the effects of EJ damage (simplified as road roughness) on the vehicle-induced dynamic response of the deck slabs of a prestressed concrete box girder bridge by using a proposed multi-degree-of-freedom vehicle model, and indicated that the EJ damage can increase the vehicle-induced impact on the deck slabs and EJ. Di et al. [11] constructed a three-dimensional numerical analysis model of an EJ system and then investigated the dynamic response and damage state of an EJ under heavy vehicle loads. Li et al. [12] carried out the field testing of 150 EJs and pointed out the diseases of EJs commonly experience, which would aggravate the vehicle-induced impact response of the EJs and the side bridge. Hou et al. [13] indicated that the height difference between the side beam and middle beam of an EJ may occur when the vertical stiffness of the main bridge and approach bridge are significantly different, and that the height difference of the EJ can significantly increase the vehicle-induced impact response of the beam end and short suspender. Ding et al. [14,15] proposed a simplified uncoupled mass–spring–damping model for a modular EJ, and analyzed the effect of varying the parameters of vehicle–bridge coupling vibration, including the gap number and gap size of the EJs. Hu et al. [16] conducted long-term monitoring of a long-span suspension bridge and clarified the dynamic response characteristics of the longitudinal movement of EJs induced by vehicles. Zhang et al. [17] used an expectation maximization algorithm method to optimize the initial parameters of EJs and applied the method to the design of EJs for a long-span bridge. Li et al. [18] analyzed the local damage effect on the natural frequencies of EJs, including the center beam, support beam, and concrete anchorage zone, and found that the natural frequencies of the center and support beams decreased with the increasing local damage.

To clarify the effect of varying the parameters of BSs on the dynamic response of vehicle–bridge coupling vibration, many researchers have conducted active experiments [19–27]. Through field testing and numerical simulation, Roeder et al. [28] pointed out that the bearing force of a BS near the beam end of a steel box girder was obviously affected by the vehicle-induced impact effect, and that BSs near the beam end were susceptible to fatigue failure under vehicle impact loads. Wang et al. [29] investigated the fatigue cracking mechanism of the BS of a half-through steel arch bridge through field testing and numerical analysis, and indicated that the vehicle-induced longitudinal displacement of the main girder mainly resulted in the fatigue cracking of the BS. Zhu et al. [30] conducted field testing of the dynamic response of vehicle–bridge coupling for a concrete girder bridge, and pointed out that the damage of BS was a susceptible disease of simply supported girder bridges, and the bearing damage may amplify the vehicle-induced dynamic response of the bridge and BS. Lu [31] carried out the damage identification of a vehicle–bridge coupling vibration system, and indicated that the local damage to a BS can significantly amplify the relevant local dynamic response of the system. Li et al. [32] conducted field testing and theoretical analysis of the vehicle-induced dynamic response of a steel tube concrete arch bridge and pointed out that damage to the BS will significantly increase the vehicle-induced impact response of the main girder, as well as the possibility of damage to the EJ. Ping et al. [33] analyzed the train-induced dynamic response of a simply supported high-speed

girder bridge through fielding testing and indicated that the variable parameters of the BS had a significant effect on the train-induced dynamic response of simply supported high-speed girder bridges. On this basis, Erduran et al. [34] developed a finite element analysis method for train–bridge coupling vibration, and then analyzed the effect of the stiffness loss of BSs on train-induced bridge vibration. The numerical results indicated that the stiffness loss of BSs can significantly increase the dynamic response of train-induced bridge vibration.

Based on the above-mentioned, the variable parameters of EJs and BSs have significant effects on the dynamic response vehicle–bridge coupling systems [35–39]. At the current stage, an analysis method for vehicle–bridge coupling vibration that considers variation of the parameters of expansion joints and bearing supports (E-B parameters) is not well developed. Recent findings mainly consider the influence of a single E-B parameter on the response of vehicle–bridge coupling vibration. An vehicle–bridge coupling vibration analysis method for curved girder bridges (considering centrifugal forces) is still lacking, and the influence of E-B parameters on the vehicle-induced vibration of curved girder bridges needs to be clarified.

In view of this, this study took a continuous curved box girder bridge as its research object, and the analysis method for the coupled vehicle–curved bridge vibration taking into account the influence of E-B parameters was proposed first by introducing a centrifugal force parameter and then verified through field testing. Subsequently, the influence of E-B parameters on the vehicle-induced dynamic responses of EJs, BSs, and curved girder bridges (MB) were investigated.

2. Analysis Method for the Dynamics Response of Vehicle–Bridge Coupling Considering Centrifugal Forces

2.1. Without Considering E-B Parameters

The vehicle body was equated to a rigid rod which was supported by the front MZ_1 and rear MZ_2 axle transient centers. The rigid rod was then supported by the vertical springs of the front and rear suspensions. The effect of centrifugal force on the wheel loads is shown in Figure 1.

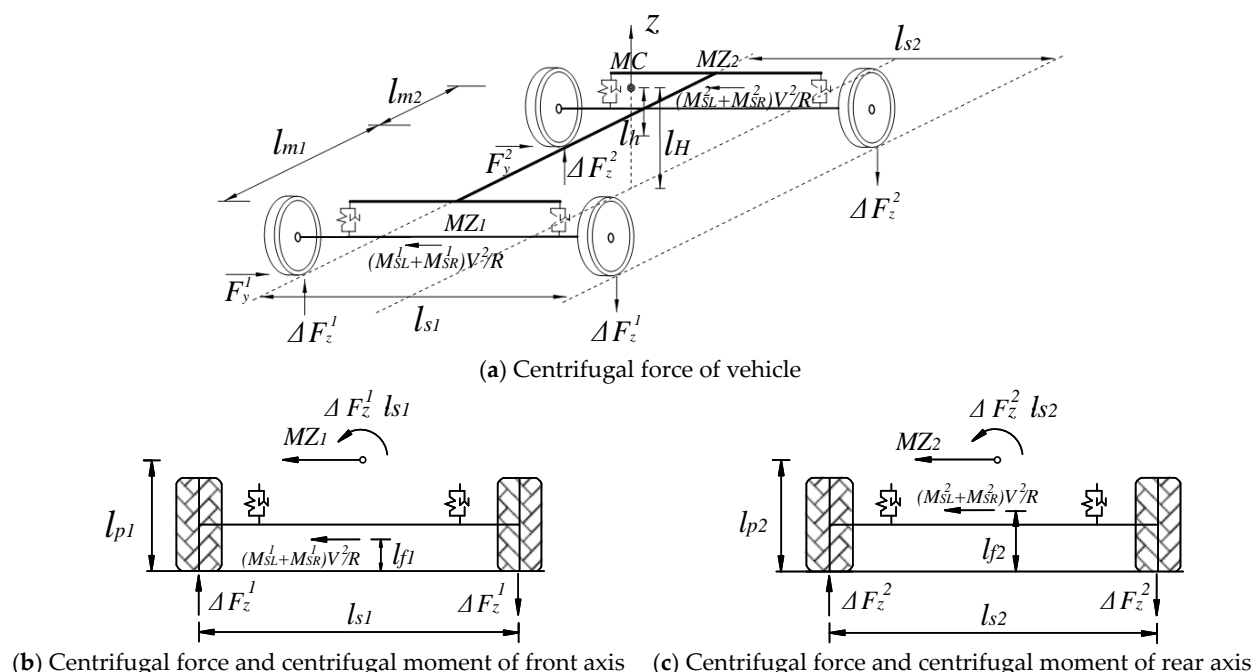


Figure 1. Effects of centrifugal force on the wheel loads.

The vehicle model moves in a uniform circle motion with a constant speed V . A centrifugal force $M_{vr}V^2/R$ acts on the center of mass, MC , of the vehicle body with mass M_{vr} , where R is the radius of curvature of the vehicle's path under uniform circular motion. This centrifugal force produces a moment $M_{vr}V^2l_h/R$ around the instantaneous axis, where l_h is the distance from MC to the instantaneous center. Since the body rotates around the instantaneous axis, its MC experiences a lateral displacement $l_h\sin\chi$ that generates an additional moment $M_{vr}gl_h\sin\chi \approx M_{vr}gl_h\chi$. The total moment is given by Equation (1) as

$$T_{vrm} = M_{vr}V^2l_h/R + M_{vr}gl_h\chi \quad (1)$$

where χ is the roll angle of the vehicle body caused by the centrifugal moment. Alternatively, the moment T_{vrm} is transmitted to the axle via the suspension spring. Given that K_{v1} and K_{v2} represent the roll angle stiffnesses of the front and rear axles, respectively, the moment T_{vrm} can also be expressed by Equation (2) as

$$T_{vrm} = (K_{v1} + K_{v2}) \cdot \chi \quad (2)$$

By combining Equation (1) with Equation (2), the roll angle of the vehicle body can be determined as shown in Equation (3).

$$\chi = \frac{M_{vr}V^2l_h/R}{K_{v1} + K_{v2} - M_{vr}gl_h} = \frac{M_{vr}l_h}{K_{v1} + K_{v2} - M_{vr}gl_h} \frac{V^2}{R} \quad (3)$$

Therefore, the spring moments of the front and rear axles can be determined, respectively as:

$$T_{vrm1} = K_{v1}\chi = \frac{K_{v1}M_{vr}l_h}{K_{v1} + K_{v2} - M_{vr}gl_h} \frac{V^2}{R} \quad (4)$$

$$T_{vrm2} = K_{v2}\chi = \frac{K_{v2}M_{vr}l_h}{K_{v1} + K_{v2} - M_{vr}gl_h} \frac{V^2}{R} \quad (5)$$

where T_{vrm1} and T_{vrm2} represent the spring moments of the front and rear axles, respectively. The centrifugal force is distributed to two instantaneous centers via the position of the center of mass. In other words, the front and rear axles distribute the centrifugal force as $M_{vr}V^2l_{m2}/[R(l_{m1} + l_{m2})]$, $M_{vr}V^2l_{m1}/[R(l_{m1} + l_{m2})]$, respectively.

The change in wheel load caused by centrifugal force is discussed using the front axle as an example. The wheel load difference ΔF_z^1 and the moment generated by the force arm l_{s1} (the distance between the left and right wheel centers of the front axle) are balanced by the sum of the three moments: (a) the spring moment T_{vrm1} of the front axle; (b) the centrifugal force $M_{vr}V^2l_{m2}/[R(l_{m1} + l_{m2})]$ distributed to the front axle and its corresponding moment formed by its force arm l_{p1} (the distance from the instantaneous center of the front axle MZ_1 to the bridge deck); (c) The moment formed by the centrifugal force acting on the front axle ($M_{sL}^1 + M_{sR}^1$) V^2/R and its corresponding force arm l_{f1} (the distance from the center of mass of the front axle MS_1 to the bridge deck). Therefore, the aforementioned moment–balance relationship can be expressed as follows:

$$\Delta F_z^1 l_{s1} = T_{vrm1} + M_{vr}V^2l_{m2}l_{p1}/[R(l_{m1} + l_{m2})] + (M_{sL}^1 + M_{sR}^1)V^2l_{f1}/R \quad (6)$$

Similarly, by considering the rear axle as an isolated system and applying the moment–balance equation, the following relationship can be established:

$$\Delta F_z^2 l_{s2} = T_{vrm2} + M_{vr}V^2l_{m1}l_{p2}/[R(l_{m1} + l_{m2})] + (M_{sL}^2 + M_{sR}^2)V^2l_{f2}/R \quad (7)$$

By combining Equations (4)–(7), the difference between the actual wheel load and the static wheel load can be expressed as follows:

$$\Delta F_z^1 = M_{vr} \frac{V^2}{R} \left(\frac{K_{v1}}{K_{v1} + K_{v2} - M_{vr} g l_h} \frac{l_h}{l_{s1}} + \frac{l_{m2}}{l_{m1} + l_{m2}} \frac{l_{p1}}{l_{s1}} + \frac{M_{sL}^1 + M_{sR}^1}{M_{vr}} \frac{l_{f1}}{l_{s1}} \right) \quad (8)$$

$$\Delta F_z^2 = M_{vr} \frac{V^2}{R} \left(\frac{K_{v2}}{K_{v1} + K_{v2} - M_{vr} g l_h} \frac{l_h}{l_{s2}} + \frac{l_{m1}}{l_{m1} + l_{m2}} \frac{l_{p2}}{l_{s2}} + \frac{M_{sL}^2 + M_{sR}^2}{M_{vr}} \frac{l_{f2}}{l_{s2}} \right) \quad (9)$$

$$F_y^1 = F_{yL}^1 + F_{yR}^1 = M_{vr} \frac{V^2}{R} \frac{l_{m2}}{l_{m1} + l_{m2}} \quad (10)$$

$$F_y^2 = F_{yL}^2 + F_{yR}^2 = M_{vr} \frac{V^2}{R} \frac{l_{m1}}{l_{m1} + l_{m2}} \quad (11)$$

where ΔF_z^1 and ΔF_z^2 denote the differences in the vertical wheel loads generated by the front and rear axles relative to the static load, respectively; ΔF_y^1 and ΔF_y^2 represent the differences in the lateral wheel load generated by the front and rear axles relative to the static load, respectively; and the subscripts *L* and *R* refer to the left and right wheels, respectively. Additionally, as the vehicle travels along a curved path, the centrifugal forces generated by the front and rear axles of the vehicle are given as follows:

$$F_{sy}^1 = F_{syL}^1 + F_{syR}^1 = (M_{sL}^1 + M_{sR}^1) \frac{V^2}{R} \quad (12)$$

$$F_{sy}^2 = F_{syL}^2 + F_{syR}^2 = (M_{sL}^2 + M_{sR}^2) \frac{V^2}{R} \quad (13)$$

Assuming that the vehicle model is undergoing uniform circular motion on a curved girder bridge, with a constant traveling speed *V* and curvature radius *R*, it follows that the magnitudes of the vertical and lateral loads induced by centrifugal force do not vary with the position of the vehicle. Rather, only the direction of the force changes as the position of the vehicle changes, while remaining constant relative to the fixed coordinate system of the vehicle model. Consequently, taking into account the effects of centrifugal force, the force applied by the left wheel to the bridge can be represented as follows:

$$\begin{Bmatrix} F_{bL}^{Ci} \\ F_{bzL}^{Ci} \end{Bmatrix} = \begin{Bmatrix} F_{byL}^{Ci} \\ F_{GL}^i + \Delta F_z^i \end{Bmatrix} = \begin{Bmatrix} F_{yL}^i + F_{syL}^i \\ F_{wzL}^i \end{Bmatrix} - \begin{Bmatrix} F_{wyL}^i \\ F_{wzL}^i \end{Bmatrix} \quad (14)$$

where the superscript *C* indicates that the effect of centrifugal force has been considered. The *n*th-order modal force F_{Bn}^C applied by the left wheel to the bridge considering the influence of centrifugal force can be represented as follows:

$$F_{Bn}^C = \sum_{i=1}^2 (\phi_h^n(x_{iL}) F_{byL}^{Ci} + \phi_v^n(x_{iL}) F_{bzL}^{Ci} + \phi_h^n(x_{iR}) F_{byR}^{Ci} + \phi_v^n(x_{iR}) F_{bzR}^{Ci}) \quad (15)$$

The equilibrium equation of vehicle–bridge coupling vibration, taking into account the effects of centrifugal force, can be presented as:

$$\begin{bmatrix} M_v & 0 \\ 0 & M_B \end{bmatrix} \begin{Bmatrix} \ddot{X}_v \\ \ddot{q}_B \end{Bmatrix} + \begin{bmatrix} C_v & C_{vB} \\ C_{Bv} & C_B + C_B^v \end{bmatrix} \begin{Bmatrix} \dot{X}_v \\ \dot{q}_B \end{Bmatrix} + \begin{bmatrix} K_v & K_{vB} \\ K_{Bv} & K_B + K_B^v \end{bmatrix} \begin{Bmatrix} X_v \\ q_B \end{Bmatrix} = \begin{Bmatrix} F_v^r \\ F_B^{CrG} \end{Bmatrix} \quad (16)$$

Within this equation, the load vector exerted by the vehicle on a curved bridge can be represented as follows:

$$F_{bn}^{CrG} = \sum_{i=1}^2 \left\{ \begin{array}{l} [k_{vlL}^i r(x_{Li}) + c_{vlL}^i r'(x_{Li})V + F_{GL}^i + \Delta F_z^i] \phi_v^n(x_{Li}) \\ + [k_{vlR}^i r(x_{Ri}) + c_{vlR}^i r'(x_{Ri})V + F_{GR}^i - \Delta F_z^i] \phi_v^n(x_{Ri}) \\ + (F_{yL}^i + F_{syL}^i) \phi_h^n(x_{Li}) + (F_{yR}^i + F_{syR}^i) \phi_h^n(x_{Ri}) \end{array} \right\} \quad (17)$$

In summary, the equilibrium equation for vehicle-bridge coupling vibration for a curved girder bridge and taking into account the effects of centrifugal force has been obtained. On this basis, further development can be undertaken to derive the equilibrium equation of vehicle-curved bridge coupling vibration considering E-B parameters.

2.2. With E-B Parameters Taken into Account

Based on Section 2.1 and the methodology for analyzing the vehicle–straight bridge coupling system whilst taking into account the expansion joint and bearing support parameters [40], the equilibrium equation for vehicle-joint (bearing-bridge coupling vibration that takes into account centrifugal force can be obtained. By incorporating the influence of centrifugal force, the force exerted on the bridge by the vehicle passing over an expansion joint at the nth-order can be expressed as follows.

$$\begin{aligned} F_{Bn}^{CrG} = & [\beta \times \phi_v^n(x_{BL,L1}) \times (F_{GL}^1 + \Delta F_z^1) + (1 - \beta) \times \phi_v^n(x_{ZL,L1}) \times (F_{GL}^1 + \Delta F_z^1)] \\ & + \beta \times \phi_v^n(x_{BL,L1}) \times k_{vlL}^1 \times [\alpha \times r(x_{BL,L1}) + (1 - \alpha) \times r(x_{ZL,L1})] \\ & + (1 - \beta) \times \phi_v^n(x_{ZL,L1}) \times k_{vlL}^1 \times [\alpha \times r(x_{BL,L1}) + (1 - \alpha) \times r(x_{ZL,L1})] \\ & + [\beta \times \phi_h^n(x_{BL,L1}) \times (F_{yL}^1 + F_{syL}^1) + (1 - \beta) \times \phi_h^n(x_{ZL,L1}) \times (F_{yL}^1 + F_{syL}^1)] \\ & + [\beta \times \phi_v^n(x_{BL,R1}) \times (F_{GR}^1 - \Delta F_z^1) + (1 - \beta) \times \phi_v^n(x_{ZL,R1}) \times (F_{GR}^1 - \Delta F_z^1)] \\ & + \beta \times \phi_v^n(x_{BL,R1}) \times k_{vlR}^1 \times [\alpha \times r(x_{BL,R1}) + (1 - \alpha) \times r(x_{ZL,R1})] \\ & + (1 - \beta) \times \phi_v^n(x_{ZL,R1}) \times k_{vlR}^1 \times [\alpha \times r(x_{BL,R1}) + (1 - \alpha) \times r(x_{ZL,R1})] \\ & + [\beta \times \phi_h^n(x_{BL,R1}) \times (F_{yR}^1 + F_{syR}^1) + (1 - \beta) \times \phi_h^n(x_{ZL,R1}) \times (F_{yR}^1 + F_{syR}^1)] \\ & + [k_{yLL}^2 \times r(x_{L2}) + c_{yLL}^2 \times r'(x_{L2}) \times V + F_{GL}^2 + \Delta F_z^2] \times \phi_v^n(x_{L2}) \\ & + [k_{yLR}^2 \times r(x_{R2}) + c_{yLR}^2 \times r'(x_{R2}) \times V + F_{GR}^2 - \Delta F_z^2] \times \phi_v^n(x_{R2}) \\ & + (F_{yL}^2 + F_{syL}^2) \times \phi_h^n(x_{L2}) + (F_{yR}^2 + F_{syR}^2) \times \phi_h^n(x_{R2}) \end{aligned} \quad (18)$$

Based on the above mentioned, for a curved bridge with EJs, when the vehicle passes over the EJs, we can use the equilibrium equation for vehicle-joint-bridge coupling vibration taking into account centrifugal force to calculate the dynamic response of the coupling using the Newmark- β method [40]. Conversely, when the vehicle passes over the bridge deck, we can use the equilibrium equation for vehicle-bridge coupling vibration, taking into account centrifugal force, to calculate the dynamic response of the coupling.

2.3. Flow Chart of the Analysis Method

The flow chart of the analysis method for vehicle-joint (bearing)-bridge coupling vibration considering centrifugal force is shown in Figure 2. As shown in Figure 2, the proposed analysis method for vehicle-joint-bridge coupling vibration that takes into account centrifugal force mainly involved three steps: Step (a), conducting numerical modeling of a curved girder bridge with EJs and EBs; Step (b), determining the modal information of a curved girder bridge with EJs and EBs, as well as vehicle parameters; and Step (c), calculating the coupled dynamic response of the vehicle-joint (bearing support)-bridge system. The detailed descriptions of the analysis method are as follows.

For Step (a), a numerical model of a bridge with EJ and EB was constructed in basis of a finite element analysis platform, and the material parameters (e.g., elastic modulus, density, and Poisson's ratio), geometrical dimensions, and the basic design parameters of EJ, EB, and a main girder were considered in detail. On this basis, the boundary conditions of the numerical model need to be clarified through testing or design parameters. For Step (b), the modal information of a curved girder bridge with EJ and EB, as well as vehicles,

was obtained on the basis of a refined finite element model and simplified vehicle model, respectively, including the mass, stiffness and the damping matrix of the EJ, EB, main girder, and vehicle. For Step (c), based on Section 2.1 and 2.2, the equilibrium equation of vehicle–joint–bridge coupling vibration that takes into account centrifugal force was used to calculate the dynamic response of the system. This analysis method was of great significance for investigating vehicle–joint–bridge coupling vibration, taking into account centrifugal force.

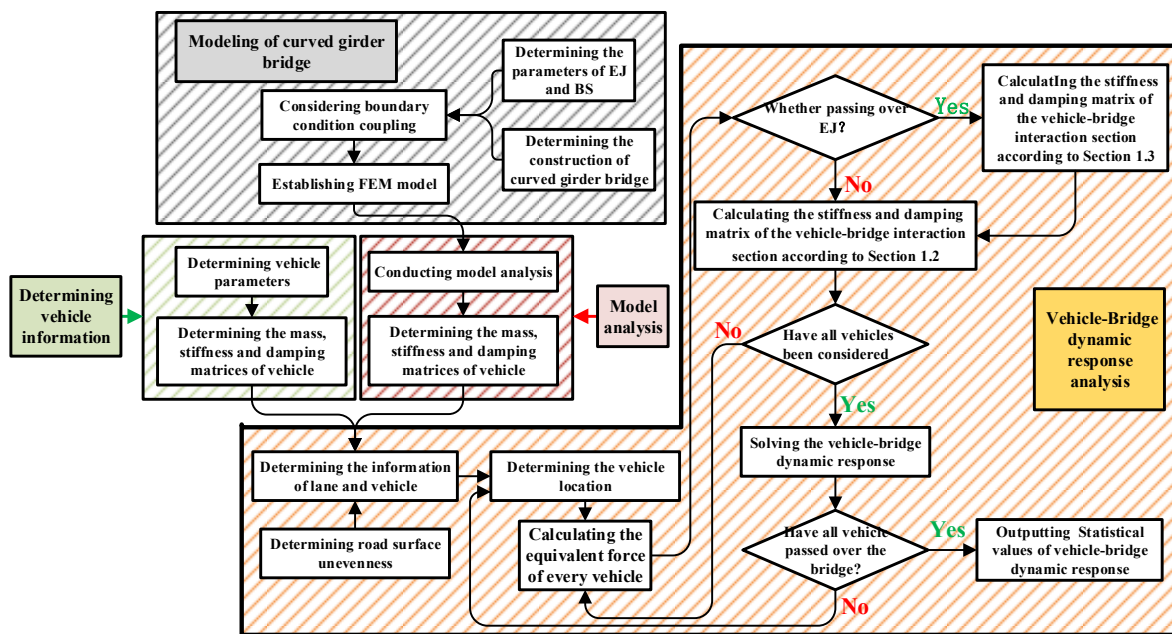


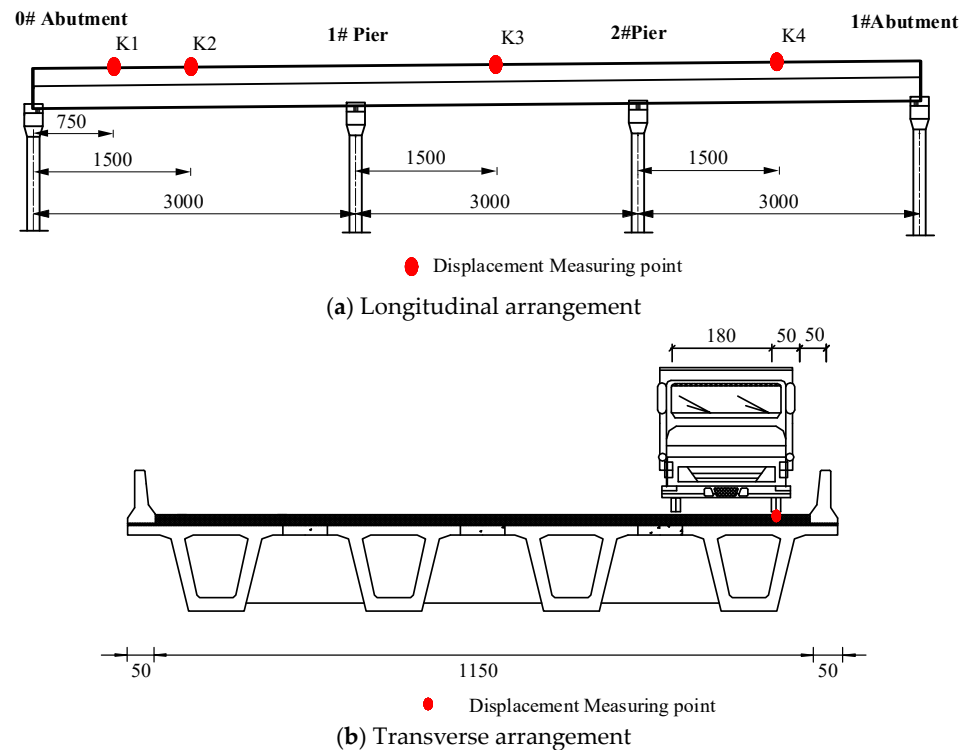
Figure 2. Flow chart of the analysis method for vehicle–joint (bearing)–bridge coupling vibration taking into account centrifugal force.

2.4. Method Validation

To validate the proposed method, the basic dynamic characteristics and vehicle-induced dynamic response of a curved continuous girder bridge were tested. The prototype bridge was a continuous curved prestressed concrete girder bridge, shown in Figure 3. The main girder of the bridge was made of four prestressed concrete single-box girders. The span arrangement of the bridge was 3×30 m. The total width of the bridge deck was 12.5 m. The concrete grade of the main girder was C50. The GQF-MZL160 double-joint modular expansion joint was installed at the beam end of the main girder. The bearing support (BS) of the bridge was a basin rubber bearing with JPZ series. The materials of the side beam, middle beam and support beam of the EJ were 16 Mn steel. The longitudinal displacement measuring points were arranged at the 1/4 point (K1) and 1/2 point (K2) of the first span, the 1/2 point (K3) of the second span, and the 1/2 point (K4) of the third span. The transverse position of each measuring point was 1 m from the outside of the deck slab. The measuring points are shown in Figure 4. Before the field testing, we inspected the technical condition of the EJ, EB, and main girder. The main detected parameters of the bridge are shown Table 1.

Table 1. Technical conditions of the EJ, EB, and main girder of the prototype bridge.

Technical Parameters	Technical Conditions
Height difference of the EJ	<2 mm, meets the design requirement
Stiffness of the EJ	Equivalent to the design parameter
Bearing capacity of the EB	Equivalent to the design parameter
Vertical stiffness of the EB	Equivalent to the design parameter
Strength of the main girder	53.1 MPa, meets the design requirement
Transverse connection conditions among main girders	Effective and without any damage
Road roughness	Close to ideal in general

**Figure 3.** Photographs of the prototype bridge.**Figure 4.** Layout of the measuring points (cm).

As shown in Table 1, in general, the technical state of the EJ, EB, and main girder was equivalent to the design state. Moreover, we can hardly adjust the actual parameters of EJ, EB, and main girder in a practical testing. In other words, during the field testing, the parameters of EJ, EB, and main girder were usually considered as constant values.

Therefore, the parameters of the finite element model were selected as the same as the design parameters during verification of the analysis model. The ANSYS platform was used to establish a refined 3D analysis model of the curved girder bridge containing EJs and BSs. The concrete box girder of the main bridge was simulated by the Solid65 element, and the BSs were established by a Combin14 element with variable stiffnesses. The middle beam, side beam, and support beam of the EJ were all simulated by the Beam188 element. The elastic support connection between the middle beam and the support beam was also simulated by the Combin14 element. The support beam was coupled with the corresponding node of the main girder to simulate the actual boundary of the support beam. The prototype of the EJ model used in this paper was a double-seam modular expansion joint (GQF-MZL160), which has been widely used in various types of bridges. This type of expansion joint included a support box (a), a side beam (b), a central beam (c), a compression support (d), a support beam (e), waterproof sealing (f), and other auxiliary components, as shown in Figure 5. The main component parameters of this type of EJ are shown in Figure 6, including a side beam (a), a central beam (b), and support beams (c and d). It should be noted that the parameters of the EJ model were strictly determined according to the actual design parameters of the prototype EJ GQF-MZL160, including Young's modulus, shear modulus, material density, Poisson's ratio, and so forth. The detail parameters of GQF-MZL160 and basin rubber bearing are shown in Table 2. The finite element model of the system is shown in Figure 7.

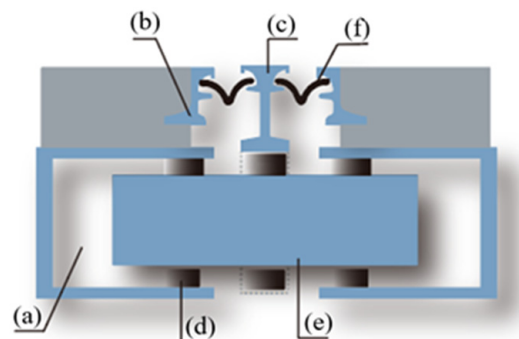


Figure 5. Diagram of the EJ, including a support box (a), a side beam (b), a central beam (c), a compression support (d), a support beam (e), a waterproof sealing (f).

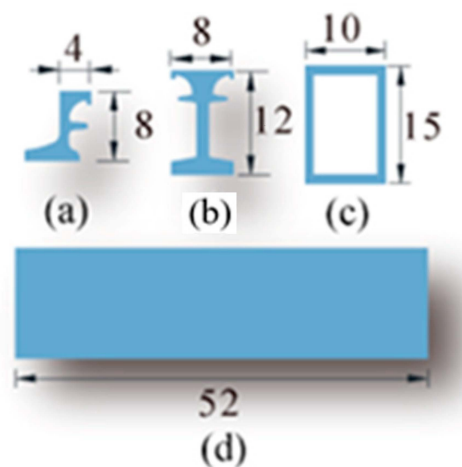
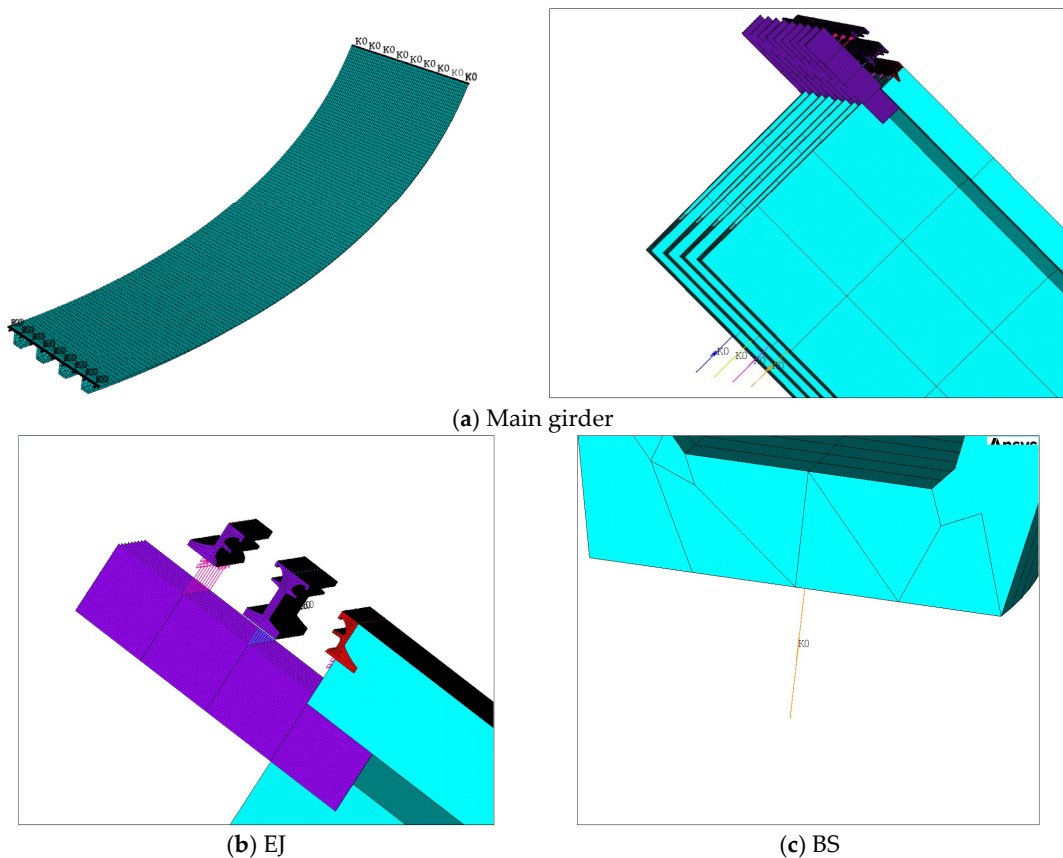


Figure 6. Section size of the main components of the EJ (cm), including a side beam (a), a central beam (b), and support beams (c and d).

Table 2. Parameters of the EJ and BS.

EJ (GQF-MZL160)		BS (GPZ2.5 DX)	
Parameters	Numerical Value	Parameters	Numerical Value
Elastic modulus E /Pa	2.05×10^{11}	Shear Modulus G /Pa	8×10^{10}
Material density ρ /(kg·m ⁻³)	7800	Poisson's ratio ν	0.2
Length of support beam L_2 /m	0.52	Length of middle beam L_1 /m	40
Width of side beam l_s /(m)	0.04	Width of middle beam l_c /(m)	0.04
Joint gap s_0 /(m)	0.08	Width of side beam h_s /(m)	0.08
Inertia moment of support beam I_2 /m ⁴	1.35×10^{-5}	Inertia moment of middle beam I_1 /m ⁴	7.7×10^{-6}
Inertia moment of side beam 1 I_2 /m ⁴	1.82×10^{-6}	Inertia moment of side beam 2 I_1 /m ⁴	1.82×10^{-6}
Support stiffness of middle beam	4×10^7	Support stiffness of support beam	2×10^8
Support damping of support beam	5000	Support damping of middle beam	5000
C_2 /(N·s) m ⁻¹		C_1 /(N·s) m ⁻¹	
Parameters		Parameters	
Design bearing capacity (kN)	2500	Design deformation capacity(mm)	± 100
Ultimate bearing capacity (kN)	2750	Sliding friction coefficient	<0.02
Vertical stiffness (kN/m)	2.4×10^6	Horizontal stiffness (kN/m)	1.5×10^5

**Figure 7.** Finite element model.

The modal information of the finite element model was obtained through the subspace iterative method, given in Table 3. As shown in Table 3, the errors of the first three vibration frequencies between the calculated and tested results were in the range of 2.26~6.32%, which indicated that the refined finite element model can well reflect the dynamic characteristics of the prototype bridge. Meanwhile, the numerical model can be applied to the subsequent numerical analysis.

Table 3. Measured and calculated modal parameters.

Modal Order	Calculation Results (Hz)	Testing Results (Hz)	Error
1	3.803	3.891	2.26%
2	4.584	4.893	6.32%
3	6.902	7.194	4.06%

Through the trial calculations, the local vibration frequencies of the EJ were mainly in the range of 82 Hz~107 Hz. The first 20 vibration modals of the main girder and 50 vibration modals of the EJ were extracted for the subsequent analysis. A two-axle truck (total weight of about 283 kN) was selected as the loading vehicle. The truck was loaded at a speed of 30 km/h along the outer lane (the outside wheel was 0.5 m from the outside of the deck slab). The specific parameters of the vehicle model are described in the literature [31]. Figure 8 shows the comparison of the numerical and field-testing results of the displacement responses of the measuring points. The comparison of the peak vertical displacements of the typical measuring points is shown in Table 4.

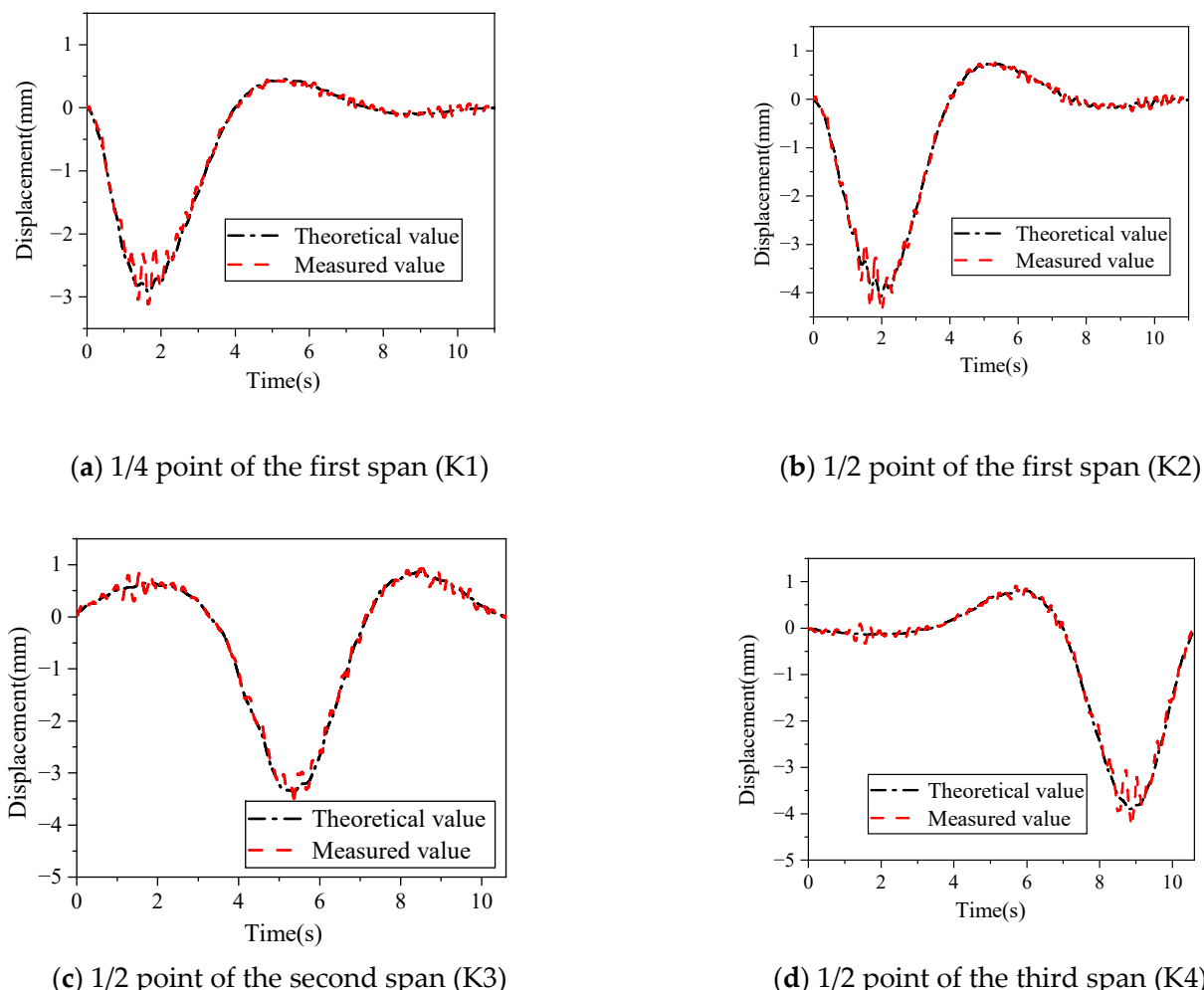
**Figure 8.** Comparison of the displacement time history curves.

Table 4. Comparison of the measured and calculated peak vertical displacements.

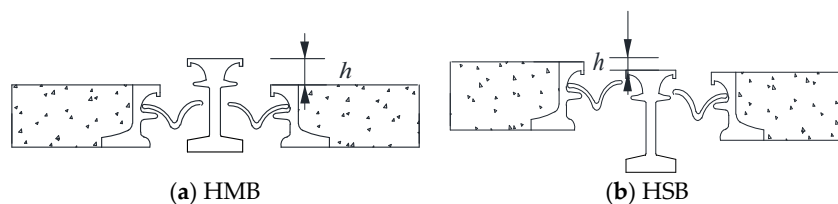
Measuring Points	Testing Values (mm)	Calculating Values (mm)	Error %
1/4 point of the first span	3.12	2.92	6.41
1/2 point of the first span	4.35	4.08	6.21
1/2 point of the second span	3.49	3.35	4.01
1/2 point of the third span	4.25	3.90	8.24

As shown in Figure 8 and Table 4, the calculated values fit well with the measured values, and the errors between the measured and calculated results were in the range of 4.01~8.24%. Because there were some differences between the actual parameters and the numerical parameters, including EJ, BS, and vehicle parameters. The numerical analysis results can be regarded as effective to some extent. Thus, the proposed method can be applied to analyze the vibration responses of the vehicle–joint (support)–bridge coupling taking into account the centrifugal force for curved girder bridges. It should be noted that the vehicle–bridge coupling vibration was characterized as nonlinear, random, and time-variable, and it was influenced by a variety of factors. The road (bridge deck) roughness was deemed as an extremely important influencing factor on the dynamic response of vehicle–bridge coupling vibration. The road (bridge deck) roughness always led to random variation in vehicle load (excitation of vehicle-induced vibration of the bridge), which in turn affected the dynamic response of the bridge. Therefore, the fluctuation of vehicle-induced vibration of the bridge increased with the deterioration of road (bridge deck) roughness, as shown in Figure 8 [41].

3. Influence of Variable Parameters of the EJ on the Vehicle-Induced Dynamic Response of the Curved Girder Bridge

3.1. Height Differences

For a double-jointed modular expansion joint, the variable parameters of the EJ mainly included: (a) height difference between the middle beam and side beam of the EJ (including the height difference between the middle beam and the two side beams, denoted as HMB, shown in Figure 9a, and the height difference between one side beam and the other side beam and the middle beam, denoted as HSB, shown in Figure 9b); (b) a reduction in the support stiffness of the support beam; and (c) the width of the joint seam—because the influence of joint width on the vehicle-induced dynamic response of bridges is relatively small. Therefore, the determined variable parameters of the EJs are shown in Table 5. It should be pointed out that the vehicle was all loaded along the outer lane for all of the simulations.

**Figure 9.** Height difference of the EJ.**Table 5.** Cases of the variable parameters of the expansion joint.

Parameters	Variable parameters of the EJ	BS parameters	Vehicle speed	Road roughness	Vehicle position	
	Height difference (mm) Support stiffness (k_0 , N/m) Seam width (mm)	-20~20 initial k_0 , 0.8 k_0 , 0.6 k_0 , 0.4 k_0 , 0.2 k_0 80	Support stiffness k_1 (N/m)	2.40×10^9	30 km/h	Ideal Outside

3.1.1. Height Difference of the Middle Beam

The support stiffness and gap size of the EJ, as well as the parameters of the BS, were set to the design values. The local road roughness (only the road roughness at the EJ was considered) was set to simulate the height difference of the middle beam (HMB). Figure 10 shows the typical vertical displacement curves over time of the individual measuring points of the bridge under different HMBs. The dynamic amplification factors (DAFs, $DAF = R_{dyn}/R_{sta} = IM + 1$) of the individual measuring points under different HMBs are shown in Figure 11.

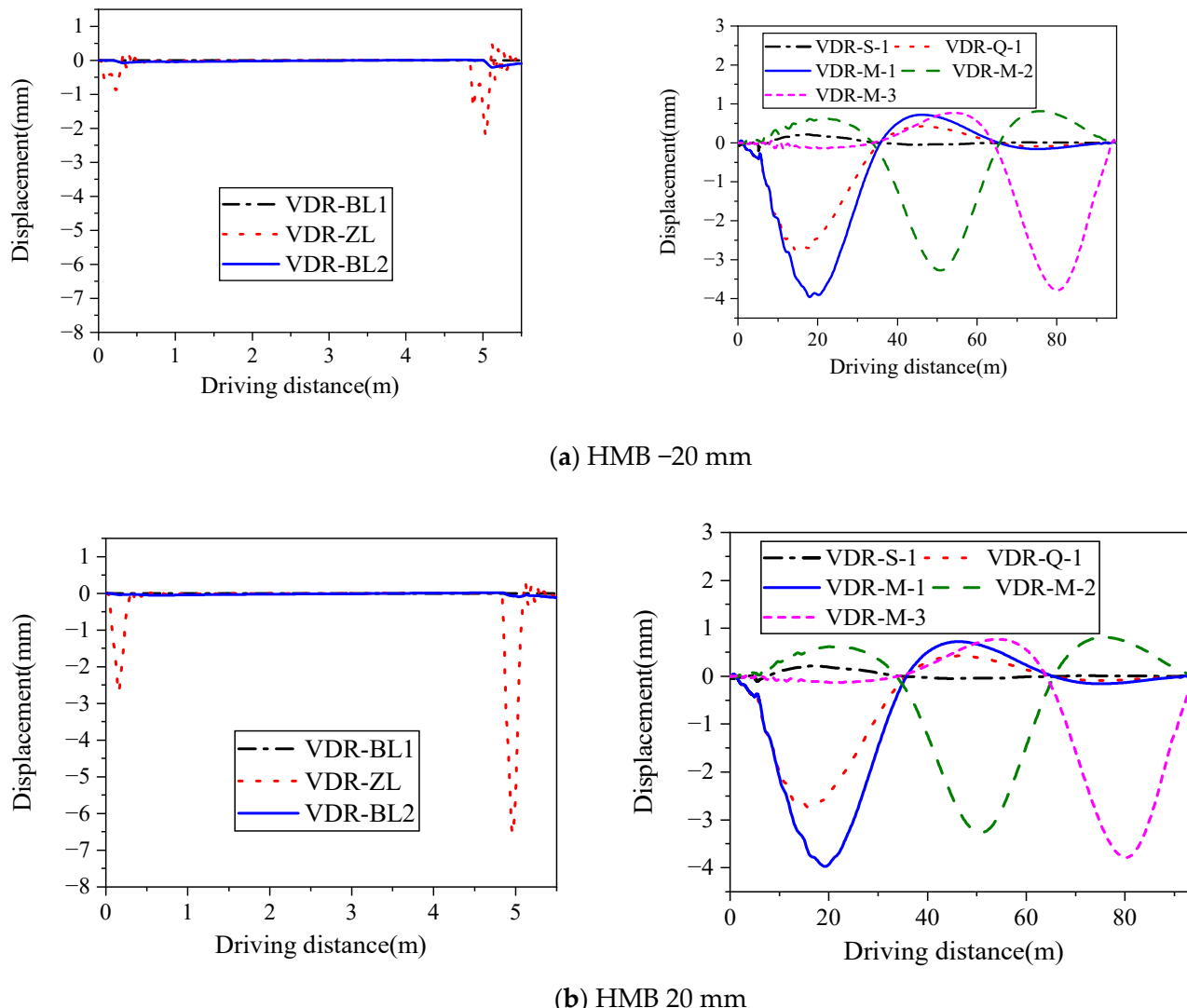


Figure 10. Displacement curves over time of the vertical displacements of individual measuring points under different HMBs (30 km/h).

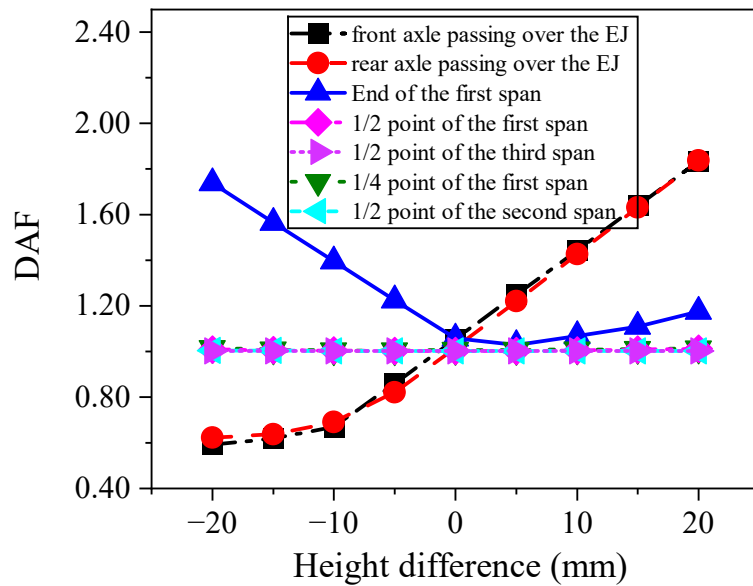


Figure 11. DAFs of individual measuring points under different HMBs (30 km/h).

As shown in Figure 11, the HMB had a significant impact on the DAFs of the EJ (DAF-EJ) and the beam end of the main girder (near the EJ). The DAF-EJ increased with increases in the HMBs. When the front and rear axles passed over the EJ, the DAF-EJ varied by -43.85% to 73.88% and -38.82% to 80.66% , with the HMB increasing from -20 mm to 20 mm, respectively, and the relevant maximum DAFs were equal to 1.834 and 1.837 , respectively. The DAFs of the beam end of the main girder tended to increase with the variation in the HMB. In other words, the increase or decrease in HMBs would both increase the DAF of the beam end, and the decrease in HMB had a more significant influence on the beam end than the increase in HMB. The max DAF was $1.739 (+64.23\%)$ with a HMB of -20 mm. The HMB had little effect on the DAF of the measuring point of the main beam far away from the EJ ($<1.0\%$). Figure 12 gives the peak variation rate of the reaction force of the 0–1# BS at the beam end (peak variation rate = variation amplitude of the reaction force with different HMBs/amplitudes of the reaction force with non-HMB) with different HMBs. The location of 0–1# was denoted as the outermost BS of the first span near the EJ.

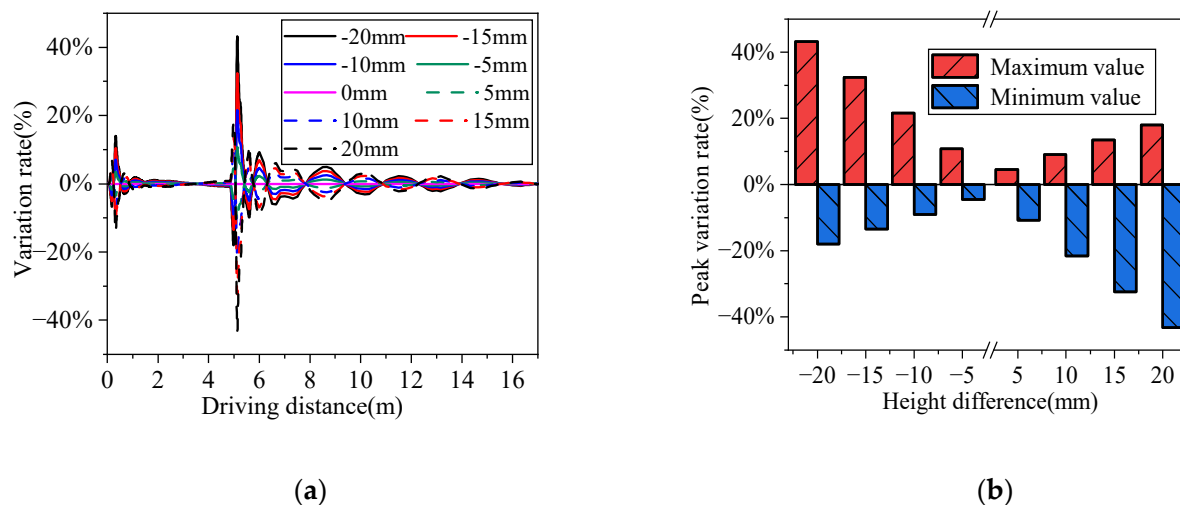


Figure 12. Variations in the reaction force of the BS with different HMBs (0–1#, 30 km/h). (a) Displacement curves over time of the variation rate of the reaction force for the BS. (b) Peak variation rate of the reaction force of the BS.

As shown in Figure 12, the peak variation rate of the reaction force of the 0–1# BS varied from -43.6% to 43.6% when the HMB varied from -20 mm to 20 mm. Thus, the variation in the HMB can result in the obvious variation in the reaction force of the BS. Accordingly, the BS can experience fatigue failure much more easily when the HMB of the EJ occurs.

3.1.2. Height Difference of the Side Beam

EJs are, in fact, more prone to HSB. Figure 13 presents the three-dimensional contours of the variation laws of the DAFs of individual measuring points.

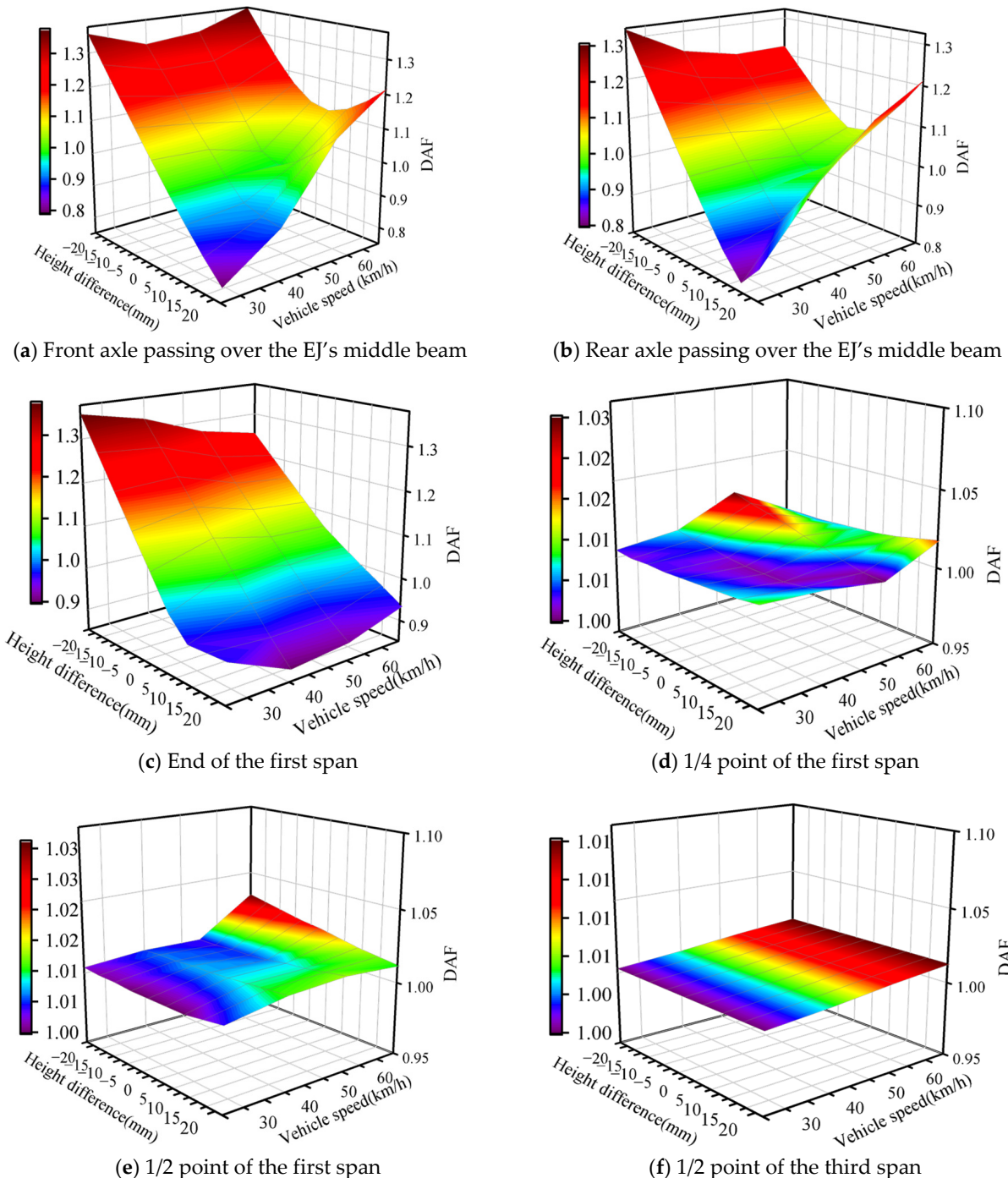


Figure 13. Variations in the DAFs with respect to vehicle speed and HSB.

Figure 13a illustrates the variations in the DAF-EJ with respect to vehicle speed and HSB when the front axle crosses the EJ. As depicted in Figure 13a, there were notable differences in DAFs with different vehicle speeds and HSBs. When the vehicle speed was low (<40 km/h), the DAF-EJ decreased steadily (from 28.44% to -24.74%) as the HSB increased from -20 mm to 20 mm. In contrast, at higher vehicle speeds (>40 km/h), the DAF-EJ increased steadily as the absolute value of the HSB increased, reaching a maximum increase of up to 31.67% .

Figure 13b illustrates how the DAF-EJ varied with respect to vehicle speed and HSB when the rear axle passed over the EJ. The observed pattern was similar to that when the front axle passes over the EJ. At low vehicle speeds, the DAF-EJ decreased as HSB increased. However, at higher vehicle speeds (>40 km/h), the DAF-EJ increased as the absolute value of HSB increased, reaching a maximum increase of up to 22.45% . By comparing this to Figure 13a,b, it can be inferred that there existed a threshold vehicle speed below which the DAF was sensitive to changes in HSB magnitude and decreased steadily as HSB increased. Above this threshold speed, however, the DAF became sensitive to changes in absolute HSB magnitude and increased steadily as the absolute HSB magnitude increased.

As shown in Figure 13c, the HSB also affected the DAF at the end of the main girder near the EJ. The DAF measured at this location decreased as the HSB increased. When HSB was -20 mm, the DAF reached its maximum value of 1.355 ; as HSB increased from -20 mm to 20 mm, the DAF increased from -24.98% to 28.00% . Furthermore, as shown in Figure 13d–f, the DAFs corresponding to the $1/4$ and $1/2$ points of the first span of the main girder, the $1/2$ point of the second span, and the $1/2$ point of the third span exhibited little sensitivity to changes in HSB. Figure 14 presents how the peak variation rate of the 0-1# BS reaction force at the beam end varied with HSB.

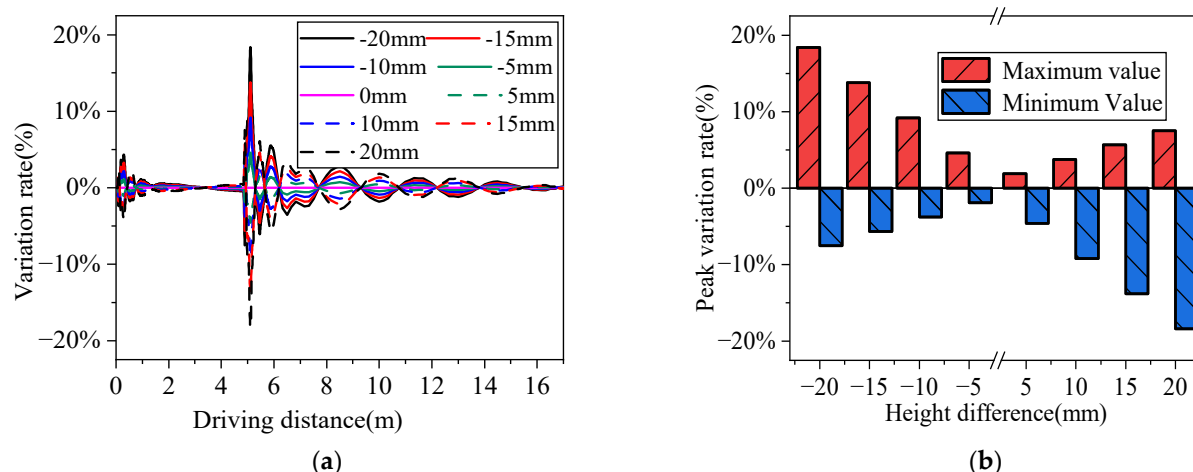


Figure 14. Variations in the BS reaction forces with different HSBs. (a) Displacement curves over time of the variation rates of the BS reaction force. (b) Peak variation rates of BS reaction force.

As shown in Figure 14, when the absolute value of HSB increased within a range of -20 mm to 20 mm, the changes in the support reaction force became more pronounced. This indicates that the possibility of fatigue failure in the support increases as the absolute value of HSB increases.

3.2. Support Stiffness of the Expansion Joints

To further investigate the effect of support stiffness of the EJs on the DAFs of different measuring points along the main girder, the height difference and width of the EJ, as well as the bearing support parameters, were all set to their respective design values. Figure 15 gives the DAFs of the bridge measurement points under different support stiffnesses of the EJ.

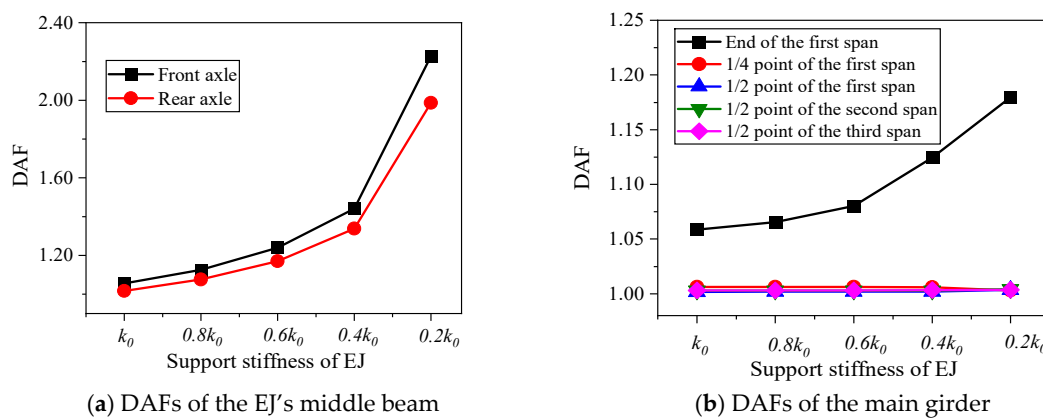


Figure 15. DAFs of the bridge measurement points under different support stiffnesses of the EJ.

According to Figure 15a, it can be observed that there was a positive correlation between the decrease in the support stiffness of the EJ and an increase in DAF-EJ. When the EJ's vertical support stiffness was reduced to $0.2 k_0$, both the front and rear axles exhibited their maximum DAF values of 2.227 and 1.987, respectively, representing increases of 111.1% and 95.4%. Furthermore, Figure 15b illustrates that, as the stiffness decreased, there was a steady increase in the DAF at the end of the main girder. At $0.2 k_0$, a maximum DAF of 1.180 was reached, corresponding to an increase of 11.4%. In addition, it was important to note that other measurement points on the main girder did not exhibit sensitivity to changes in the vertical support stiffness of the EJ. The change rule of the variation rate of the 0–1# BS reaction force with the support stiffness of the EJ is shown in Figure 16.

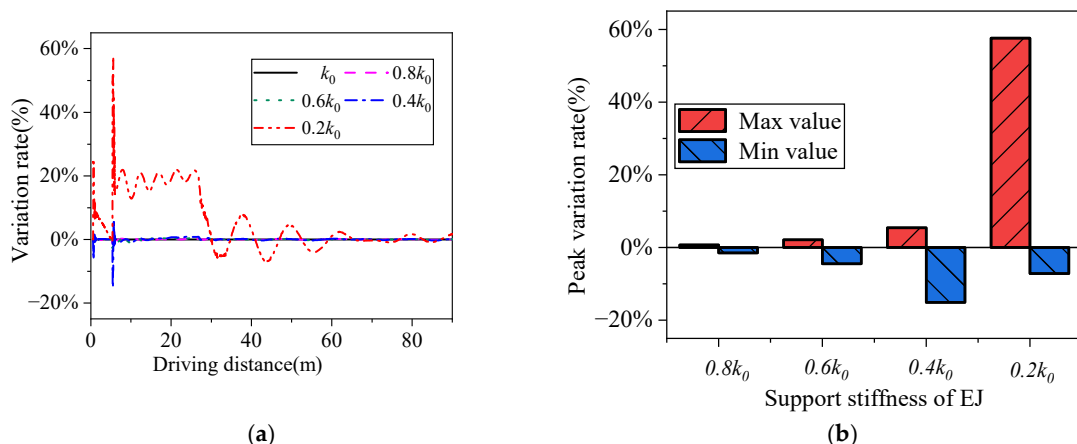


Figure 16. Variations in the BS reaction forces with different support stiffnesses of EJ. (a) Displacement curves over time of the variation rate of the 0–1# BS reaction force. (b) Peak variation rate of BS reaction force.

According to Figure 16, it can be observed that there was a positive correlation between the decrease in the EJ's vertical support stiffness and an increase in the BS reaction force. The range of the increases was between -15.14% and 57.53% . As the degradation of EJ's vertical support stiffness intensified, there was a corresponding increase in impact on the BS from vehicles, which may lead to fatigue and other forms of damage to the BS.

4. Effects of Support Variable Parameters on the Vehicle-Induced Responses of Curved Girder Bridges

To clarify the effects of variations in BS parameters on bridge safety, two common issues of BSs, stiffness reduction and support voiding, were considered in this section. A reduction in the stiffness of the BS can easily be simulated by altering the equivalent

spring stiffness of the BS. For the sake of generality in this research, we assumed that only 0-1# BS experienced a stiffness reduction. In terms of support voids, both single- and double-support void scenarios were designed. The support void was simulated by removing the relevant spring at the corresponding BS. The detailed layout of the BSs is shown in Figure 17. The parameter settings for each working condition analysis model are presented in Table 6; meanwhile, the working conditions designed to study support voids are shown in Table 7.

Table 6. Parameter settings for each working condition analysis model.

	Parameters of EJs	Support parameters		Vehicle speed	Unevenness of the road surface	Lateral position of the vehicle
Parameters	Height difference (mm)	0	Vertical support stiffness of the support	Intact $k_1, 0.8 k_1, 0.6 k_1, 0.4 k_1, 0.2 k_1$ (0 abutment 1#)	30 km/h	Ideal
	Support stiffness (k_0 , N/m)	8.00×10^7		Void condition (support stiffness is 0 and the main girder is not in contact with the support)		
	Seam width (mm)	80	Support void			Outside

Table 7. Working conditions for support void analysis.

Parameters of	Working Conditions of Voids
Single-Support Void	0-1#, 0-2#, 0-3#, 0-4#, 1-1#, 1-2#, 1-3#, 1-4# 0-1, 2# 0-1, 3# 0-2, 3# 0-2, 4# 1-1, 2# 1-1, 3# 1-2, 3# 1-2, 4#
Double-Support Void	0-4#, 1-4# 0-4#, 1-4# 0-4#, 2-4# 1-4#, 1-4# 1-4#, 2-4# 2-4#, 1-4#

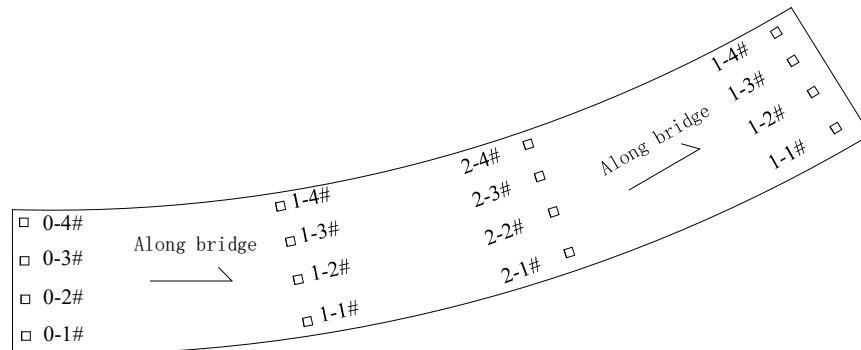


Figure 17. Layout of supports.

4.1. Reduction in BS Stiffness

The curves of the changes in the DAFs at various measurement points under the working conditions of a bearing support stiffness reduction are shown in Figure 18.

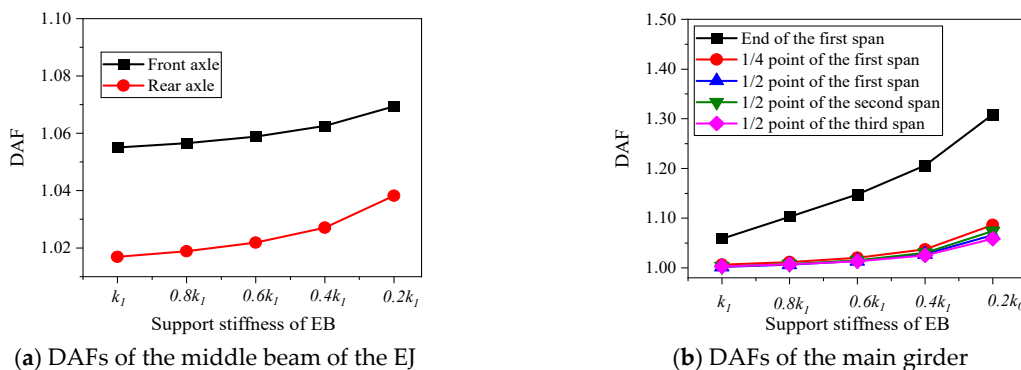


Figure 18. DAF curves of the bridge measuring points under different bearing support vertical stiffnesses.

As illustrated in Figure 18a, when the front and rear axles pass over the EJ, there is an increase in the DAF-EJ corresponding to a reduction in the 0–1# BS vertical stiffness. The maximum increase rates of DAFs were 1.35% and 2.10% for the front and rear axles passing over, respectively. This suggests that a reduction in BS stiffness has a relatively small impact on the DAF-EJ. However, Figure 18b shows that the DAF at each measurement point on the main girder exhibited a steady increase as the 0–1# BS support stiffness decreased. At a BS support stiffness value of 0.2 k_0 , the maximum increase rates in the DAFs at the end of the first span, the 1/4 point of the first span, the 1/2 point of the first span, the 1/2 point of the second span, and the 1/2 point of the third span were 24.18%, 7.97%, 6.40%, 7.10%, and 5.51%, respectively. This indicates that changes in BS stiffness have a significant impact on the DAFs at various measurement points on the main girder, especially the beam end of the first span.

4.2. Support Voids

4.2.1. Single-Support Void

The changes in the DAFs at various measurement points under single-support void conditions are shown in Figure 19.

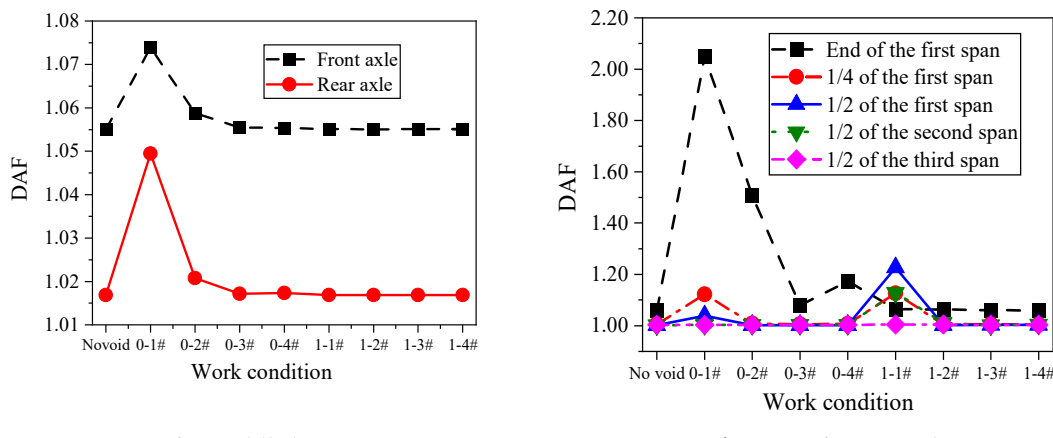


Figure 19. DAFs at bridge measurement points under different single void conditions.

As illustrated in Figure 19a, there was a relatively large impact on the DAF-EJ when single supports 0–1# and 0–2# were voided. When the front axle passed over the EJ, the increases in the DAF-EJ were 1.80% and 0.38%, respectively. Similarly, when the rear axle passed over EJ, the increase rates in the DAF-EJ were 3.15% and 0.39%, respectively. The impact of other single-support voids on the DAF-EJ was negligible. This indicates that DAF-EJ is not sensitive to a single-support void.

As illustrated in Figure 19b, the DAFs of individual measurement points of the main girder were significantly affected by the support void within and adjacent to the span. For instance, when single supports 0–1#, 0–2#, 0–3#, or 0–4# were voided, the increase rates in DAFs at the end of the main girder were 29.27%, 18.13%, 1.89%, and 7.27%, respectively. Notably, when 0–1# or 0–2# were voided, the DAF at the end of the main girder exceeded the design value (1.220) by a considerable margin.

4.2.2. Double-Support Void

The DAFs at various measurement points under double-support void conditions are summarized in Table 8.

Table 8. DAFs of the bridge measurement points with different double-support voids at 30 km/h.

Working Condition of Double Support Void	Category	Measurement Points						
		Front Axle Passing over EJ Middle Beam	Rear Axle Passing over EJ Middle Beam	End of the First Span	1/4 Point of the First Span	1/2 Point of the First Span	1/2 Point of the Second Span	1/2 Point of the Third Span
The support is intact	DAF	1.055	1.017	1.059	1.006	1.002	1.003	1.003
		0-1, 2#	1.082	1.102	1.548	1.447	1.131	1.003
		0-1, 3#	1.074	1.050	1.403	1.124	1.039	1.003
		0-1, 4#	1.075	1.056	1.431	1.159	1.053	1.003
		0-2, 3#	1.059	1.021	1.239	1.008	1.002	1.003
		0-2, 4#	1.059	1.021	1.229	1.008	1.003	1.003
		0-3, 4#	1.056	1.018	1.132	1.007	1.004	1.003
		1-1, 2#	1.055	1.016	1.024	1.305	1.534	1.417
		1-1, 3#	1.055	1.017	1.065	1.126	1.227	1.129
		1-1, 4#	1.055	1.017	1.066	1.127	1.230	1.138
		1-2, 3#	1.055	1.017	1.067	1.003	1.004	1.014
		1-2, 4#	1.055	1.017	1.064	1.004	1.003	1.013
		1-3, 4#	1.055	1.017	1.051	1.004	1.006	1.007
		0-4, 1-4#	1.074	1.050	1.385	1.264	1.277	1.130
		0-4, 2-4#	1.074	1.049	1.377	1.121	1.040	1.192
		0-4, 1-4#	1.074	1.050	1.382	1.122	1.039	1.039
		1-4, 2-4#	1.055	1.017	1.057	1.129	1.233	1.375
		1-4, 1-4#	1.055	1.017	1.020	1.127	1.228	1.129
		2-4, 1-4#	1.055	1.017	1.021	1.004	1.002	1.193

As presented in Table 8, three main conclusions can be drawn. (a) A double-support void had a relatively small (less than 10%) impact on the DAF-EJ. (b) Compared to a single-support void, a double-support void had a more significant impact on the DAF of the beam end of the main girder. When double supports 0–1, 2# and 0–4#, 1–4# were voided, the increase rates in DAFs at the end of the main girder were 46.2% and 30.5%, respectively, and both maximum DAFs exceeded the design value (1.220). (c) The variation in the DAF of the middle span point of the main girder due to a double-support void was much more significant than that due to the single-support void. The maximum DAFs at the 1/4 and 1/2 points of the first span, the 1/2 point of the second span, and the 1/2 point of the third span were 1.447, 1.534, 1.417, and 1.235, respectively, and the corresponding increase rates reached 43.84%, 53.09%, 41.28%, and 23.13%, respectively. In conclusion, a double-support void can result in significant changes in the DAFs of the main girder, which can significantly compromise bridge safety.

5. Impact of Coupled Changes in the E-B Parameters on Dynamic Responses of Curved Girder Bridges to Vehicular Loads

5.1. Orthogonal Experimental Design

To further investigate the impacts of coupled changes in E-B parameters on the dynamic responses of curved girder bridges to vehicular loads, a sensitivity analysis was conducted using the orthogonal experimental design. Four factors were considered for sensitivity analysis: HMB, EJ vertical support stiffness, bearing support stiffness, and support voiding. Each factor was evaluated at three levels, resulting in the $L_9(3^4)$ orthogonal table, presented in Table 9.

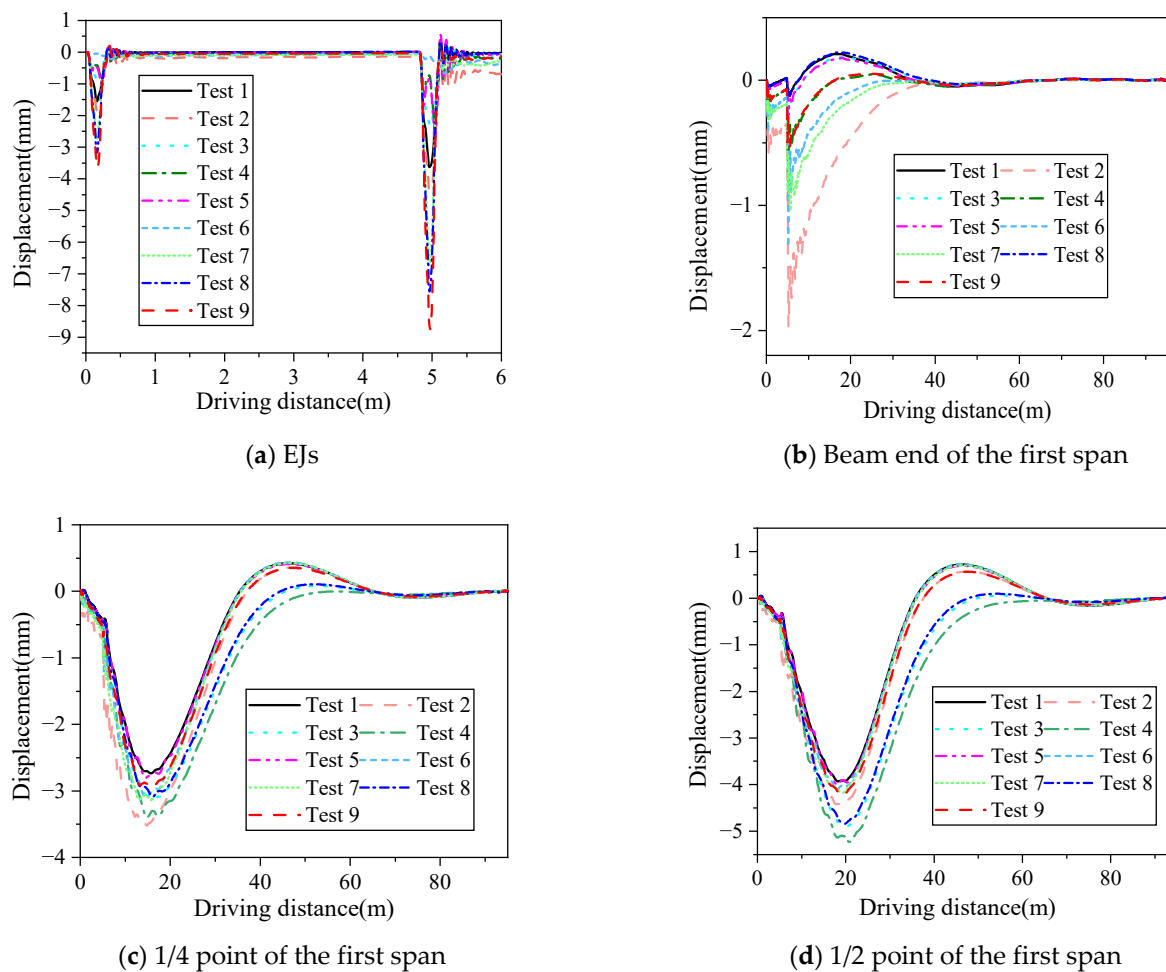
Table 9. Scheme of the orthogonal numerical simulation test.

Numbering of Orthogonal Tests	Factor 1	Factor 2	Factor 3	Factor 4
1	0 mm	k_0	k_1	No void
2	0 mm	$0.6 k_0$	$0.2 k_1$	0 abutment 1#
3	0 mm	$0.2 k_0$	$0.6 k_1$	1 span 1#
4	-20 mm	k_0	$0.2 k_1$	1 span 1#
5	-20 mm	$0.6 k_0$	$0.6 k_1$	No void
6	-20 mm	$0.2 k_0$	k_1	0 abutment 1#
7	20 mm	k_0	$0.6 k_1$	0 abutment 1#
8	20 mm	$0.6 k_0$	k_1	1 span 1#
9	20 mm	$0.2 k_0$	$0.2 k_1$	No void

Note: k_0 is the design support stiffness of EJ; k_1 is the design support stiffness of BS.

5.2. Coupled Parameter Influence Analysis

As illustrated in Figure 20, the dynamic responses of the bridge became more complex when coupled changes in E-B parameters were considered. To provide a more intuitive understanding of the effects of various factors on the DAFs at different measurement points, Figure 21 presents a comparison of the sensitivities for DAF at various measurement points concerning four influencing factors.

**Figure 20. Cont.**

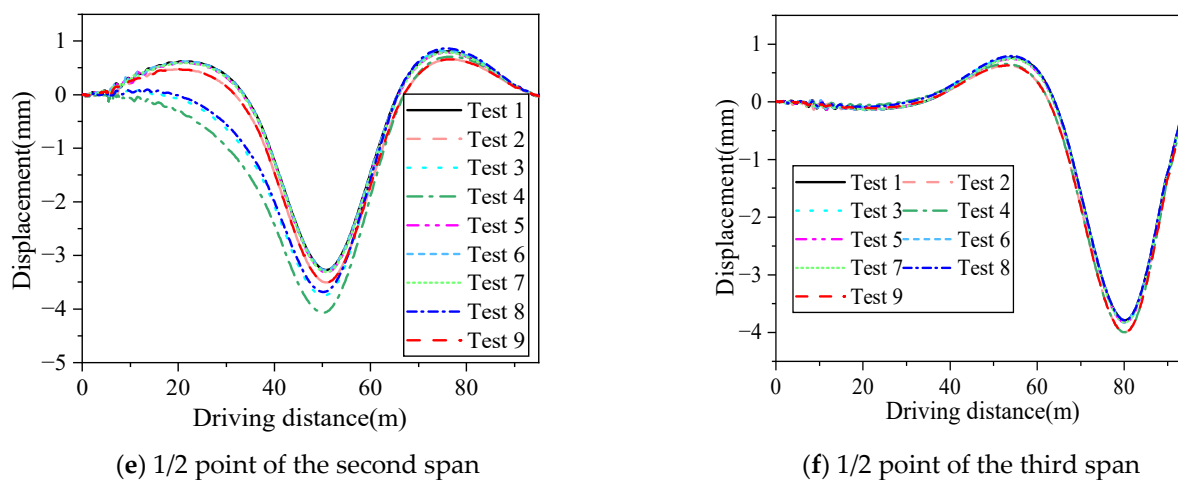


Figure 20. Displacement curves over time of the bridge measuring points.

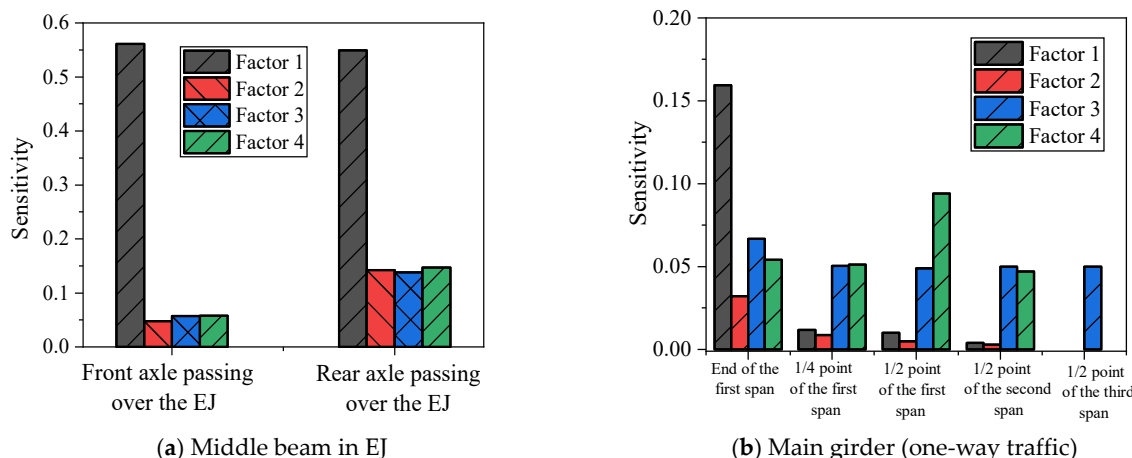


Figure 21. Sensitivity comparison of the individual measuring points.

As Figures 20 and 21 show, the DAFs-EJ exhibited a significantly higher sensitivity to the variations in BMS compared to the variations in BS support stiffness, EJ vertical support stiffness, or support voiding. Additionally, the DAFs-EJ exhibited a significantly higher sensitivity to variations in these four parameters when the rear axle passed over the EJ. Also, the sensitivity of the four impact factors to the DAF changed with variations in the positions of the main girder. For the end of the first span, the order of sensitivities was BMS > support void > BS support stiffness > EJ vertical support stiffness; for the 1/4 and 1/2 points of the first span, the order of sensitivities was support void > BS support stiffness > EJ vertical support stiffness > BMS; and for the 1/2 point of the second span, the order of sensitivities was BS support stiffness > support void > BMS > EJ vertical support stiffness. It should be noted that, for the 1/2 point of the third span, the sensitivity of four impact factors to the DAF at this measurement point depended on traffic passing one-way over the bridge. When considering one-way traffic, the DAF at the 1/2 point of the third span only showed sensitivity to changes in BS support stiffness at the ends of this span. When considering two-way traffic, the sensitivity of the four impact factors to the DAF at this point was the same as that of the first span.

It should be noted that certain EJ and BS parameters were given in the finite element models in this study, and the loading vehicle was selected as a two-axle truck, which only travelled along the outside lane of the bridge with ideal road roughness. Therefore, systematic numerical analyses of the vehicle–joint (bearing support)–bridge coupling vibration need to be carried out by taking into account the variable parameters of curved

bridges, vehicles, and so forth. Moreover, rapid technical condition evaluation methods for the EJ, BS, and main girder based on variation in the dynamic response of vehicle–joint (bearing support)–bridge coupling vibration are also a hotspot for future study.

6. Conclusions

In this study, an analysis method for the dynamic response of a vehicle–joint (bearing)–bridge coupling, taking into account the centrifugal force, was proposed and verified based on field testing data. Subsequently, a continuous curved box girder bridge was taken as a research object to investigate the influence of variable parameters of the expansion joints and bearing supports on the vehicle-induced dynamic responses of the curved girder bridge. The main findings are summarized as follows:

- (1) The proposed analysis method can be applied to analyze the vehicle-induced dynamic response of a curved girder bridge, taking into account the variable parameters of expansion joints (EJs) and bearing supports (BSs). The errors between the theoretical analysis results and the field-testing results were in the range of 4.01~8.24%.
- (2) The DAF of the middle beam of an expansion joint (DAF-EJ) increased with the increase of its relevant height difference; the DAF of the beam end of the main girder increased with increasing or decreasing relevant height difference. There was a speed limitation which made the DAFs-EJ increase with the increasing height difference of the side beam, while the DAF of the beam end decreased with the increasing relevant height difference. The DAFs of the middle beam and the beam end both significantly increased with the decreasing support stiffness of the EJ. The height difference and support stiffness reductions to the EJ will both significantly vary the bearing reaction force of the BS, and may result in the fatigue failure of the BS.
- (3) The DAFs of the middle beam of the EJ and the main girder increased with the support stiffness reduction in the BS near the beam end of the main girder. The reduction in the support stiffness of the BS had little effect on the DAF-EJ, but had a significant effect on the DAF of the main girder, especially the beam end. The DAFs of the middle beam of the EJ, the beam end, the 1/4 and 1/2 points of the first span, as well as the 1/2 point of the second span, were obviously influenced by the single-support void near the traffic lane or corresponding measurement points. Moreover, the DAFs of the middle beam of the EJ and the main girder were more influenced by the double-support void, especially the beam end of the main girder.
- (4) The DAF-EJ was more sensitive to the height difference of the middle beam of the EJ and the vertical support stiffness variation in the BS and EJ. The DAF of the beam end of the main girder was most sensitive to the height difference of the middle beam of the EJ. The influences of the height difference of the middle beam of the EJ on the DAFs of the beam end, the 1/4 and 1/2 points of the first span, as well as the 1/2 points of the second and third spans, gradually decreased. The DAF of the beam end of the main girder was most significantly affected by the reduction in support stiffness.

Author Contributions: Conceptualization, Y.Z., C.L., X.H., W.X. and D.Z.; Methodology, C.L. and L.H.; Software, Y.Z., X.H., J.L. (Jianxiang Li), L.H. and Y.S.; Validation, Y.Z., C.L., J.L. (Jin Li), L.H. and K.W.; Formal analysis, X.H. and J.L. (Jianxiang Li); Investigation, Y.Z. and W.X.; Resources, X.H., W.X., D.Z., J.L. (Jin Li), K.W. and Y.S.; Data curation, D.Z.; Writing—original draft, J.L. (Jianxiang Li); Writing—review & editing, W.X. All authors have read and agreed to the published version of the manuscript.

Funding: This research was funded by the National Natural Science Foundation of China (Grant Nos. 52108428, 52178446, 51978021, 51908015) and the Beijing Natural Science Foundation (Grant No. 8232001).

Data Availability Statement: The raw data supporting the conclusions of this article will be made available by the authors on request.

Conflicts of Interest: Author Yu Zheng was employed by the company China Railway Beijing Group Co., Ltd. Authors Daxing Zhou, Jin Li, Liqun Hou, Kuan Wang and Yulong Sun were employed by the company China Railway Construction Group Co. Ltd. The remaining authors declare that the research was conducted in the absence of any commercial or financial relationships that could be construed as a potential conflict of interest.

References

- Li, N.; Xu, W.; Chen, Y.; Yan, W. Experimental research on adjacent pounding effect of midspan curved bridge with longitudinal slope. *Eng. Struct.* **2019**, *196*, 109320. [\[CrossRef\]](#)
- Sha, B.; Xing, C.; Xu, J.; Wang, H.; Li, A. A novel orthogonally separated isolation system and its seismic performance on a curved concrete bridge. *Int. J. Struct. Stab. Dyn.* **2021**, *21*, 2150158. [\[CrossRef\]](#)
- Li, Z.; Kang, S.; You, C. Seismic mitigation of curved continuous girder bridge considering collision effect. *Symmetry* **2022**, *14*, 129. [\[CrossRef\]](#)
- McCarthy, E.; Wright, T.; Padgett, J.E.; DesRoches, R.; Bradford, P. Development of an experimentally validated analytical model for modular bridge expansion joint behavior. *J. Bridge Eng.* **2014**, *19*, 235–244. [\[CrossRef\]](#)
- Jiao, C.; Liu, W.; Wu, S.; Gui, X.; Huang, J.; Long, P.; Li, W. Shake table experimental study of curved bridges with consideration of girder-to-girder collision. *Eng. Struct.* **2021**, *237*, 112216. [\[CrossRef\]](#)
- Ramos, Ó.; Schanack, F.; Carreras, G.O.; Retuerto, J.d.V. Bridge length limits due to track-structure interaction in continuous girder prestressed concrete bridges. *Eng. Struct.* **2019**, *196*, 109310. [\[CrossRef\]](#)
- Sun, Z.; Siringoringo, D.M.; Fujino, Y. Load-carrying capacity evaluation of girder bridge using moving vehicle. *Eng. Struct.* **2021**, *229*, 111645. [\[CrossRef\]](#)
- Artmont, F.A.; Roy, S. A model for simulating dynamic vehicular load on modular bridge expansion joint systems. In Proceedings of the 8th World Congress on Joints, Bearings, and Seismic Systems for Concrete Structures Georgia, Transportation Research Board, Atlanta, GA, USA, 25–29 September 2016.
- Deng, L.; Yand, W.; Zhu, Q. Vehicle impact on the deck slab of concrete box-girder bridges due to damaged expansion joints. *J. Bridge Eng.* **2016**, *21*, 06015006. [\[CrossRef\]](#)
- Deng, L.; Cao, R.; Wang, W.; Yin, X. A multi-point tire model for studying bridge–vehicle coupled vibration. *Int. J. Struct. Stab. Dyn.* **2016**, *16*, 1550047. [\[CrossRef\]](#)
- Di Mascio, P.; Loprencipe, G.; Moretti, L.; Puzzo, L.; Zoccali, P. Bridge expansion joint in road transition curve: Effects assessment on heavy vehicles. *Appl. Sci.* **2017**, *7*, 599. [\[CrossRef\]](#)
- Lima, J.M.; De Broto, J. Inspection survey of 150 expansion joints in road bridges. *Eng. Struct.* **2009**, *31*, 1077–1084. [\[CrossRef\]](#)
- Hou, J.; Xu, W.; Chen, Y.; Zhang, K.; Sun, H.; Li, Y. Typical diseases of a long-span concrete-filled steel tubular arch bridge and their effects on vehicle-induced dynamic response. *Front. Struct. Civ. Eng.* **2020**, *14*, 867–887. [\[CrossRef\]](#)
- Ding, Y.; Xie, X.; Au, F.T.; Huang, J. Analysis of dynamic load of vehicle bumping at bridge-head using distributed spring-damper element (in Chinese). *China Civ. Eng. J.* **2012**, *45*, 127–135.
- Ding, Y.; Zhang, W.; Au, F.T. Effect of dynamic impact at modular bridge expansion joints on bridge design. *Eng. Struct.* **2016**, *127*, 645–662. [\[CrossRef\]](#)
- Hu, J.; Wang, L.; Song, X.; Sun, Z.; Cui, J.; Huang, G. Field monitoring and response characteristics of longitudinal movements of expansion joints in long-span suspension bridges. *Measurement* **2020**, *162*, 107933. [\[CrossRef\]](#)
- Zhang, Y.-M.; Wang, H.; Bai, Y.; Mao, J.-X.; Chang, X.-Y.; Wang, L.-B. Switching Bayesian dynamic linear model for condition assessment of bridge expansion joints using structural health monitoring data. *Mech. Syst. Signal Process.* **2021**, *160*, 107879. [\[CrossRef\]](#)
- Li, J.; Wen, F.; Chen, J.; Yang, C.; Du, W.; Xu, L.; Li, P. Experimental study of bridge expansion joint damage based on natural frequency. *Sensors* **2023**, *23*, 6437. [\[CrossRef\]](#)
- EN 1337-1; Structural Bearings—Part 1 General Design Rules. European Committee for Standardization (CEN): Brussels, Belgium, 2000.
- TB10621—2014; Code for Design of High Speed Railway. China Railway Publishing House: Beijing, China, 2015.
- Wei, W.; Yuan, Y.; Igarashi, A.; Zhu, H.; Tan, P. Experimental investigation and seismic fragility analysis of isolated highway bridges considering the coupled effects of pier height and elastomeric bearings. *Eng. Struct.* **2021**, *233*, 111926. [\[CrossRef\]](#)
- Aria, M.; Akbari, R. Inspection, condition evaluation and replacement of elastomeric bearings in road bridges. *Struct. Infrastruct. Eng.* **2013**, *9*, 918–934. [\[CrossRef\]](#)
- Cui, M.; Wu, G.; Dang, J.; Chen, Z.; Zhou, M. Deep learning-based condition assessment for bridge elastomeric bearings. *J. Civ. Struct. Health Monit.* **2022**, *12*, 245–261. [\[CrossRef\]](#)
- Ma, F.; Zhang, L.; Cui, M.; Cheng, X.; Zou, Y.; Cui, Y.; Wu, G. Investigation and treatment of bearing diseases for typical expressway and high-speed railway bridges in Eastern China: A field practice campaign. *Struct. Infrastruct. Eng.* **2022**, *20*, 13–35. [\[CrossRef\]](#)
- Freire, L.M.; De Brito, J.; Correia, J.R. Inspection survey of support bearings in road bridges. *J. Perform. Constr. Facil.* **2015**, *29*, 04014098. [\[CrossRef\]](#)

26. Ma, F.; Li, H.; Hou, S.; Kang, X.; Wu, G. Defect investigation and replacement implementation of bearings for long-span continuous box girder bridges under operating high-speed railway networks: A case study. *Struct. Infrastruct. Eng.* **2022**, *18*, 678–693. [[CrossRef](#)]
27. Freire, L.M.; De Broto, J.; Correia, J.R. Management system for road bridge structural bearings. *Struct. Infrastruct. Eng.* **2014**, *10*, 1068–1086. [[CrossRef](#)]
28. Roeder, C.W.; MacRae, G.; Crocker, P.; Arima, K.; Wong, S. Dynamic response and fatigue of steel tied-arch bridge. *J. Bridge Eng.* **2000**, *5*, 14–21. [[CrossRef](#)]
29. Wang, Q.; Okumatsu, T.; Nakamura, S.; Nishikawa, T.; Wu, Q.; Chen, K. Fatigue failure analysis of cracks near the sole plate of a half-through steel-arch bridge. *J. Bridge Eng.* **2019**, *24*, 05019004. [[CrossRef](#)]
30. Zhu, X.Q.; Law, S.S. Damage detection in simply supported concrete bridge structure under moving vehicular loads. *J. Vib. Acoust.* **2007**, *129*, 58–65. [[CrossRef](#)]
31. Lu, Z.; Liu, J.; Huang, M.; Xu, W. Identification of local damages in coupled beam systems from measured dynamic responses. *J. Sound Vib.* **2009**, *326*, 177–189. [[CrossRef](#)]
32. Li, Y.; Cai, C.S.; Liu, Y.; Chen, Y.; Liu, J. Dynamic analysis of a large span specially shaped hybrid girder bridge with concrete-filled steel tube arches. *Eng. Struct.* **2016**, *106*, 243–260. [[CrossRef](#)]
33. Hu, P.; Zhang, C.; Chen, S.J.; Wang, Y.; Wang, W.; Duan, W.H. Dynamic responses of bridge–embankment transitions in high speed railway: Field tests and data analyses. *Eng. Struct.* **2018**, *175*, 565–576. [[CrossRef](#)]
34. Erduran, E.; Nordli, C.; Gonen, S. Effect of elastomeric bearing stiffness on the dynamic response of railway bridges considering vehicle–bridge interaction. *Appl. Sci.* **2022**, *12*, 11952. [[CrossRef](#)]
35. Busel, A.; Krotau, R. The design and composition of expansion joints on big-span bridges with intensive heavy-duty traffic. *Transp. Res. Procedia* **2016**, *14*, 3953–3962. [[CrossRef](#)]
36. Dexter, R.J.; Osberg, C.B.; Mutziger, M.J. Design, specification, installation, and maintenance of modular bridge expansion joint systems. *J. Bridge Eng.* **2001**, *6*, 529–538. [[CrossRef](#)]
37. Fu, C.C.; Zhang, N. Investigation of bridge expansion joint failure using field strain measurement. *J. Perform. Constr. Facil.* **2011**, *25*, 309–316. [[CrossRef](#)]
38. Sun, Z.; Zhang, Y. Failure mechanism of expansion joints in a suspension bridge. *J. Bridge Eng.* **2016**, *21*, 05016005. [[CrossRef](#)]
39. Zhang, X.; Cheng, Z.; Du, L.; Du, Y. Progressive classifier mechanism for bridge expansion joint health status monitoring system Based4040 on acoustic sensors. *Sensors* **2023**, *23*, 5090. [[CrossRef](#)]
40. Hou, J.; Wang, J.; Xu, W.; Chen, Y.; Wang, B.; Liu, J.; Shen, B.; Li, Y.; Sun, H. An analysis method of vehicle–bridge coupling vibration considering effects of expansion joint parameters and its application. *Struct. Control Health Monit.* **2022**, *29*, e3065. [[CrossRef](#)]
41. Zhang, X.; Chen, E.; Li, L.; Si, C. Development of the dynamic response of curved bridge deck pavement under vehicle–bridge interactions. *Int. J. Struct. Stab. Dyn.* **2022**, *22*, 2241003. [[CrossRef](#)]

Disclaimer/Publisher’s Note: The statements, opinions and data contained in all publications are solely those of the individual author(s) and contributor(s) and not of MDPI and/or the editor(s). MDPI and/or the editor(s) disclaim responsibility for any injury to people or property resulting from any ideas, methods, instructions or products referred to in the content.